JOURNAL OF GEOPHYSICAL RESEARCH, VOL. 106, NO. D5, PAGES 4845–4870, MARCH 16, 2001

New model for the vapor growth of hexagonal ice crystals in the atmosphere

Stephen E. Wood and Marcia B. Baker

Geophysics Program, University of Washington, Seattle

Donna Calhoun[1]

Department of Applied Mathematics, University of Washington, Seattle

Abstract. We present a new microphysical model for the vapor growth and aspect ratio evolution of faceted, hexagonal ice crystals in the atmosphere. Our model is based on a novel, efficient numerical method for solving Laplace's equation for steady state diffusion on the surface of a three-dimensional hexagonal prism, and also takes into account the surface kinetic processes of crystal growth. We do not include ventilation, so our model is limited to stationary crystals or falling crystals smaller than 100 μm. We calculate a self-consistent solution for the distribution of the supersaturation and the condensation coefficient on each crystal face, for several different assumptions regarding the crystal growth mechanism and ice surface properties. We use this model to predict the aspect ratios expected for faceted ice crystals over a range of temperatures and supersaturations, as well as to estimate the conditions for which faceted growth becomes unstable and the crystals become hollowed or dendritic. We compare these predictions to observed features of ice cloud crystals to infer some microphysical characteristics of ice crystals and their temperature dependence. We also compare our predicted mass growth rates with those of the capacitance model for spheres and ellipsoids to look at the effects of shape and surface kinetics. Finally, we insert the single-particle code into a simple parcel cloud model to investigate the feedbacks between crystal surface kinetics, shape, and the thermodynamic properties of clouds.

1. Introduction: Habit Evolution in Vapor-Grown Ice Crystals

The shapes of ice crystals in the atmosphere, and the physical processes that determine them, have long been subjects of great interest, not only because of their importance for radiative transfer [*Vogelmann and Ackerman*, 1995; *Baker*, 1997] and cloud particle dynamics [*Jensen et al.*, 1994b], but also because of their inherent beauty and complexity [*Frank*, 1982]. The primary growth habit, or shape, of a faceted ice crystal is a hexagonal prism with two basal faces and six prism faces. The aspect ratio is defined as $\Gamma \equiv c/a$, where $2c$ is the height, or distance between the basal faces, and $2a$ is the width, or distance between opposite prism faces. Many laboratory and field observations have found that the aspect ratio and habit of a vapor-grown crystal depend on the ambient temperature (T_∞) and supersaturation (σ_∞). Planar crystals ($\Gamma < 1$) form when $T_\infty > -4$°C or -10°C$> T_\infty > -22$°C, and columnar crystals ($\Gamma > 1$) form when -4°C$> T_\infty > -10$°C or $T_\infty < -22$°C. At a given temperature, observed crystal shapes are increasingly lacunar or dendritic at higher supersaturations: Columns develop hollows at each end, and plates typically have six separate arms or branches. These observational results have been summarized in a number of habit diagrams, for example the *Kobayashi* [1965] diagram shown in Figure 1, which all show similar shape variations as a function of temperature and supersaturation [*Nakaya et al.*, 1958; *Mason*, 1971; *Magono and Lee*, 1966]. However, there are also observations which do not fit neatly into these diagrams. Hexagonal ice crystals collected from the atmosphere at temperatures below -22°C often consist of a mixture of plates and columns [*Curry et al.*, 1990; *Heymsfield et al.*, 1990; *Korolev et al.*, 1999]. It is difficult to interpret these observations because in the atmosphere crystals may experience different temperature regimes during growth

[1]Now at Department of Computer Science, Courant Institute of Mathematical Sciences, New York University, New York.

Paper number 2000JD900338.
0148-0227/01/JD900338 $09.00

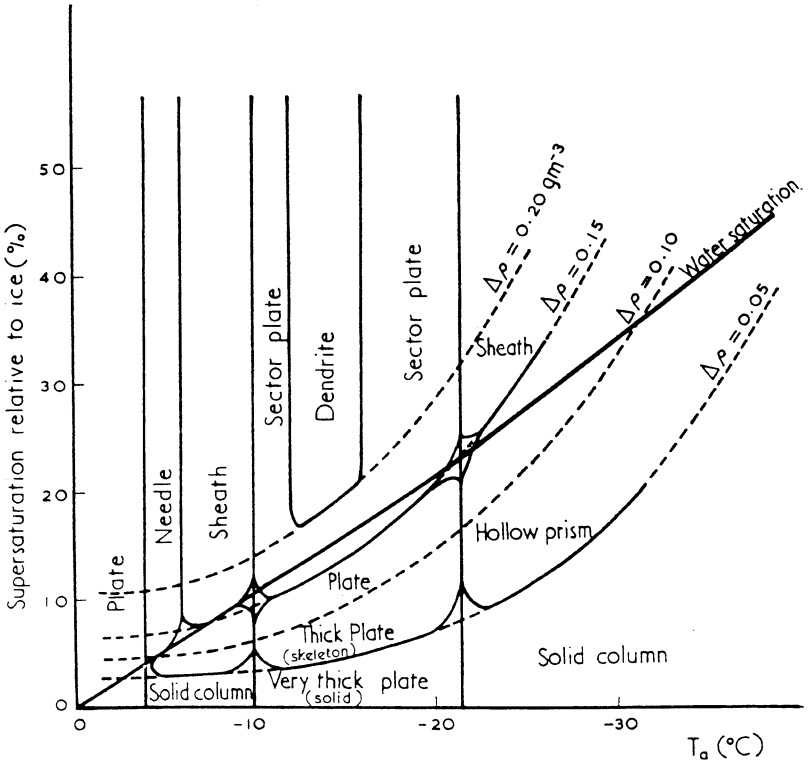

Figure 1. Habit diagram, based on laboratory observations, reproduced from *Kobayashi* [1961].

due to sedimentation and transport. However in a laboratory study of ice particles grown at constant temperatures, suspended in an electrodynamic balance [*Bacon et al.*, 2000], plate-like crystals predominate between -20°C and -40°C, where most habit diagrams indicate columns. Ice crystals with $\Gamma \geq 10$ have been observed in clear-sky precipitation in Antarctica, together with three, four, five, and six-sided plates at temperatures around -35°C [*Kikuchi and Hogan*, 1979]. We should also note that many of the larger ice particles found in the atmosphere are aggregates of many individual crystals (snowflakes), or polycrystalline with a common origin (bullet rosettes, side planes) [e.g., *Heymsfield et al.*, 1990], but in this paper we will consider only single crystals.

The primary physical processes responsible for both the shape and growth rate of an ice crystal are (1) macroscopic processes such as vapor and heat diffusion in the environment surrounding the crystal and (2) molecular-scale surface processes of incorporation of the vapor molecules into the crystal. Secondary processes such as ventilation and coagulation may become important for large ice crystals, but will not be considered in this paper due to the difficulties already involved in modeling diffusion and surface kinetics for three-dimensional hexagonal crystal growth. Numerical models of the distributions of diffusing quantities outside an object of complex shape tend to be unwieldy and slow. More important, the molecular-scale physics of the incorporation process is not well understood, and we have very few measurements of the microscopic surface parameters over the tropospherically relevant temperature range. In most ice crystal growth models in the atmospheric literature, crystal shapes are usually approximated as ellipsoids of fixed, or temperature-dependent aspect ratio, and the surface kinetics are neglected. *Yokoyama and Kuroda* [1989] presented a model in which crystal surface kinetics and shape evolution are treated in detail, but only for two-dimensional crystals. More recently, *Libbrecht* [1999] has developed an interesting method for modeling the growth of three-dimensional cylindrical crystals which includes a parameterized treatment of surface kinetics, but he has not explicitly modeled the crystal growth mechanism(s) or included latent heating effects.

Although it is not yet possible to construct a complete theory or even a general numerical model of the vapor growth of ice crystals, the importance of this process in the atmosphere motivates us to take the first step by constructing a simplified model, in which we (1) consider only simple, faceted crystal shapes and (2) use empirical values for ice surface parameters whose temperature dependence is not understood. Because the accuracy and completeness of this empirical data are limited, we have tried to strike a balance in the presentation of our model predictions, using the available data when possible to make our "current best guess", but also stating our results in terms of the parameters that are now uncertain, in order that new and improved measurements can be used in the future to

refine our predictions. Our model is based on earlier crystal growth models with coupled diffusion and surface kinetics [*Nelson*, 1994; *Nelson and Baker*, 1996; *Wood*, 1999] combined with a novel, efficient numerical method for solving Laplace's equation on the surface of a three-dimensional hexagonal prism developed for this application primarily by one of us (D. C.).

The goals of this paper are (1) to present an efficient numerical model for calculation of the evolution of single, vapor-grown faceted ice crystals, (2) to delineate the thermodynamic regimes in which ice crystals are expected to grow as faceted crystals, (3) to infer microphysical growth processes from observed crystal shapes, and (4) to insert the single-particle code into a simple cloud model and test its predictions against those of simpler ice crystal growth models.

In section 2 we present the mathematical problem of faceted crystal growth, describe our numerical method for its solution, and discuss the limitations of the model. In section 3 we describe the surface kinetic processes and microphysical input parameters that determine the condensation coefficients. In section 4 we present some model results including the calculated distributions of supersaturation and condensation coefficient on the surfaces of three-dimensional hexagonal crystals and their linear and mass growth rates. We compare our predicted mass growth rates with those of two other ice crystal growth models commonly used in cloud models, namely, the equivalent sphere and capacitance models. We also use our model to predict the growth shapes expected for crystals with different assumed growth mechanisms in a range of environments and to define the conditions for stability of faceted crystals. In section 5 we apply these results to observed features of crystals in clouds to infer microphysical characteristics of ice crystals at low temperatures where some parameters have not been measured (below $-15°$C). We use the inferred microphysical parameters and our model to derive in section 6 the first model-predicted habit diagram for the range $-30°\text{C} \leq T \leq 0°\text{C}$, for several different assumptions regarding the operative crystal growth mechanism(s). In section 7 we insert the single-particle growth code into a simple parcel cloud model to investigate the feedbacks between crystal surface kinetics, crystal shape, and the thermodynamic properties of clouds. A summary and discussion of our results are given in the final section.

2. The Mathematical Model and Numerical Solution

2.1. Modeling Ice Crystal Growth From the Vapor

Consider an ice crystal growing in an environment at ambient temperature T_∞, total pressure p, vapor pressure e_∞, and supersaturation σ_∞, where the subscript ∞ indicates parameter values far from the crystal. The ambient vapor mixing ratio is given by

$$q_\infty = \frac{\mu_{vapor}}{\mu_{air}} \frac{e_\infty}{(p - e_\infty)}, \simeq 0.622 \frac{e_{eq}(T_\infty)}{p} (1 + \sigma_\infty), \quad (1)$$

where μ is molecular weight and e_{eq} is the equilibrium vapor pressure of ice, assumed here to be much less than p. The growing crystal is a sink for water vapor and reduces the vapor mixing ratio in the vicinity of the crystal. For stationary ice crystals, we have quasi-steady state diffusion and the vapor field obeys Laplace's equation,

$$\nabla^2 q = 0. \quad (2)$$

For faceted growth the vapor flux to the crystal is uniform along each face [*Nelson*, 1994]. For notational convenience we use the subscript i to number the crystallographically distinct faces. For symmetric crystals, there are two classes of faces; $i = 1$ corresponds to the basal, or c faces, and $i = 2$ corresponds to the prism, or a faces. Then the condition of uniform flux to the ith face can be expressed as

$$\rho_{air} D_v(T,p) \frac{\partial q}{\partial n} = F_{v,i}, \qquad i = 1,2, \quad (3)$$

where ρ_{air} is the density of air, $\partial(\ )/\partial n$ denotes differentiation with respect to the direction normal to the surface, and the flux values $F_{v,i}$ are unspecified constant scalars representing the vapor flux to the two sets of crystal faces. $D_v(T,p)$ (m^2/s) is the vapor diffusivity, given by

$$D_v(T,p) \equiv 2.0 \times 10^{-5} \left(\frac{T}{T_0}\right)^{1/2} \frac{p_0}{p}, \quad (4)$$

where $T_0 = 273.13°$ K and $p_0 = 101,300$ Pa [*Pruppacher and Klett*, 1997]. For each set of environmental conditions, we assume a uniform value of $D_v(T,p)$, computed using $T = T_\infty$ and a constant pressure p, assumed to be the ambient pressure. For notational convenience this constant value will be referred to as simply $D_v \equiv D_v(T_\infty, p)$.

These equations provide flux (or Neumann) boundary conditions of the form

$$\frac{\partial q}{\partial n} = \frac{F_{v,i}}{\rho_{air} D_v}, \qquad \text{on face } i,\ i = 1,2, \quad (5)$$

for (2).

To determine the unknown constants $F_{v,i}$, we require that the flux rate of vapor due to diffusion of vapor to the crystal surface equal the rate of molecular incorporation due to kinetic processes on the surface. At each point $\mathbf{x} = (x,y,z)$ on the crystal surface, this condition can be expressed as

$$\rho_{air} D_v \frac{\partial q}{\partial n} = \rho_{air} q_{eq}(T(\mathbf{x}),p) \frac{\overline{v}_{th}}{4} \alpha_i(\sigma(\mathbf{x}))\sigma(\mathbf{x}), \quad (6)$$

where the left-hand side is an expression for the diffusive vapor flux and the right-hand side an expression for the kinetic vapor flux. The functions $\alpha_i(\sigma)$, $i = 1, 2$, are the condensation coefficients for each face which will be derived in section 3, and $\overline{v}_{th}$ is the component of the thermal velocity of the molecules directed toward the crystal surface (given by $\sqrt{8kT/\pi m}$). The variable $\sigma(\mathbf{x})$ is the spatially varying surface supersaturation, given by

$$\sigma(\mathbf{x}) = \frac{q(\mathbf{x}) - q_{eq}(T(\mathbf{x}), p)}{q_{eq}(T(\mathbf{x}), p)}. \tag{7}$$

Since we are imposing a uniform flux across each face, we have only two unknown flux values, $F_{v,1}$ and $F_{v,2}$, to determine. Therefore we impose the flux condition (6) at only two locations on the crystal surface. Mathematically, attempting to impose (6) at more than two locations would lead to an overdetermined system of equations for the unknown fluxes $F_{v,i}$. Physically, requiring the condition to hold on more than one location on each face would imply that the growth rate of the face is controlled by vapor fluxes at more than one location, contradicting our assumption of uniform faceted growth. Owing to the symmetry of the crystal, it is sufficient to choose a set of symmetric points $\mathbf{x}_1^*$ on each of the c faces and $\mathbf{x}_2^*$ on each of the a faces at which we will impose condition (6). We will henceforth label all variables at these points by an asterisk.

Imposing (6) at the two sets of locations $\mathbf{x}_i^*$ and manipulating (6) leads to an equation of the form

$$\frac{\partial q}{\partial n} = \frac{q_{eq}(T_i^*, p)\,\overline{v}_{th}}{4D_v}\,\alpha_i^*(\sigma_i^*)\,\sigma_i^*, \qquad i = 1, 2, \tag{8}$$

where for simplicity we write σ_i^* instead of $\sigma(\mathbf{x}_i^*)$. If we view the fluxes $F_{v,i}$ as unknowns and use equation (5), we can determine values $F_{v,i}$ which lead to a solution of Laplace's equation (2) which satisfies (8) at the two locations $x_i^*, i = 1, 2$. In section 2.2 we will describe in detail how we numerically determine these unknown flux values $F_{v,i}$.

2.1.1. Temperature variations at the surface of the crystal. Phase change at the crystal surface liberates latent heat, which modifies the temperature near the crystal surface and thus the local supersaturation. For this reason we also want to be able to determine the spatial distribution of the temperature field on the crystal surface. As with the mixing ratio q, the rate of heat diffusion to the crystal surface happens on a much faster timescale than the growth of the crystal, so we can assume that for the purposes of computing flux rates to the surface, the temperature field is in quasi-steady state and satisfies

$$\nabla^2 T = 0. \tag{9}$$

Furthermore, we make the assumption that the diffusion of heat in the crystal is much faster than in the vapor, and thus that the bulk crystal is isothermal and that temperature variations on the surface are not reflected in the bulk crystal. This is a common assumption that allows us to avoid the more complicated problem of solving for temperature in both the crystal and surrounding environment.

The far-field temperature is given by T_∞, and the boundary conditions at the crystal surface are given in terms of the conductive heat flux $F_{T,i}$ to each face. This flux can be related to the vapor flux $F_{v,i}$ by the expression

$$L_{sub}F_{v,i} + F_{T,i} = 0, \qquad i = 1, 2, \tag{10}$$

where L_{sub} (J kg^{-1}) is the latent heat of sublimation, and $F_{v,i}$ (kg m^{-2} s^{-1}) is the diffusive vapor flux discussed in the previous section. We can write the flux $F_{T,i}$ in terms of the normal derivative of the temperature as

$$F_{T,i} = \kappa\frac{\partial T}{\partial n}, \qquad \text{on face } i,\ i = 1, 2, \tag{11}$$

where κ (W m^{-1} K^{-1}) is the thermal conductivity of the surrounding air. Using (10) and (11), we find that on the ith faces

$$\begin{aligned}\frac{\partial T}{\partial n} &= \frac{-L_{sub}}{\kappa}F_{v,i} \\ &= \frac{-L_{sub}\,\rho_{air}\,D_v}{\kappa}\,\frac{\partial q}{\partial n},\end{aligned} \tag{12}$$

so that on the crystal surface the temperature field $T(\mathbf{x})$ can be written directly in terms of $q(\mathbf{x})$:

$$T(\mathbf{x}_i) - T_\infty = \frac{-L_{sub}\rho_{air}D_v}{\kappa}(q(\mathbf{x}_i) - q_\infty). \tag{13}$$

The spatially varying temperature is used in the computation of $q_{eq}(T, p)$, which in turn shows up in the calculations of σ.

2.1.2. Growth rates of faces. Once we have computed the fluxes $F_{v,i}$, it is a straightforward matter to compute the growth velocities of the ith face:

$$V_i = \frac{1}{\rho_{ice}}F_{v,i}. \tag{14}$$

This growth velocity will then be used to advance the interface in a manner described in more detail in the following section.

2.2. A Numerical Solution Method

We wish to solve (2) subject to the surface boundary conditions (3) for the full three-dimensional hexagonal crystal. While analytic solution methods are feasible for simpler shapes, such as the ellipsoid or cylinder, a fully numeric method must be used for the general hexagonal prism. The two main issues involved in determining the evolution of the crystal shape are (1) solving Laplace's equation on the hexagonal three-dimensional crystal, and (2) determining the correct flux conditions $F_{v,i}$.

2.2.1. A boundary integral representation. Since we are interested in values of q and fluxes only on the surface of the crystal, we formulate Laplace's equation as an integral along the boundary of the crystal surface and solve for the unknown values $q(x, y, z)$ on the surface directly. From a numerical point of view, the boundary integral approach is convenienent because we can handle arbitrary geometries in a straightforward manner and, in principle, achieve solutions of arbitrarily high order of accuracy. Furthermore, when solving exterior problems, boundary integral methods have the advantage that we do not need to impose boundary conditions on an artificial far-field boundary. Other methods such as finite difference or finite element methods would require that one approximate the far-field boundary at a boundary of a finite computational domain.

The boundary integral representation of the general exterior problem $\nabla^2 q = 0$, subject to $\partial q/\partial n = f$ over a piecewise smooth surface S is given by

$$2\pi q(P) + \int_S q(P') \frac{\partial}{\partial n_{P'}} \left[\frac{1}{|P - P'|}\right] dS_{P'} + [2\pi - \Omega(P)]\, q(P) = \int_S f(P') \frac{1}{|P - P'|}\, dS_{P'}, \quad (15)$$

where $\Omega(P)$ is the inner solid angle of S at $P \in S$. Points P and P' are points on the surface S, $|P - P'|$ is the distance between P and P', and the derivative $\partial(\ )/\partial n_{P'}$ is the difference with respect to the normal at point P'. This formulation can also be viewed as a Dirichlet-Neumann map which takes, in our case, Neumann (flux) data and produces the Dirichlet (value) data which satisfy Laplace's equation. The solution to the above problem assumes homogenous far-field boundary conditions. Adding q_∞ to the above solution yields a solution with the proper nonzero far-field conditions and that still satifies Laplace's equation and the given flux boundary conditions on the surface of the crystal.

To solve this equation, we use BIEPACK [*Atkinson*, 1999], a package written specifically to solve boundary integral equations on piecewise smooth surfaces. This package creates and refines a triangulation of the piecewise smooth boundary and solves the general integral equation using collocation methods over these triangles. Figure 2 shows a triangulation of the c and a faces. As the triangulation is refined, the size of the linear system that results from the discretization of the integral equation can become quite large. To solve this system efficiently, BIEPACK uses a two grid iteration strategy, described by *Atkinson* [1994]. Other methods for solving the integral equation (15) in three space dimensions include the fast multipole method (FMM) of *Greengard and Rohklin* [1997]. This method has been shown to give very accurate results on extremely complicated geometries. The only drawback to the FMM is that it is tedious to code, and, currently, no software is readily available.

2.2.2. Determining flux values $F_{v,i}$. To compute the fluxes $F_{v,i}$, we need to satisfy equation (8). To do this, we set up a nonlinear system $\mathbf{G}(F_{v,i})$, where the ith entry is given by

$$G_i(F_{v,1}, F_{v,2}) \equiv \frac{F_{v,i}}{\rho_{air}\, D_v} - \frac{q_{eq}(T_i^*, p)\, \overline{v}_{th}}{4 D_v}\, \alpha_i^*(\sigma_i^*)\, \sigma_i^*. \quad (16)$$

A description of how to evaluate the system $\mathbf{G}$ is given in Figure 3. In that subroutine we require values $q(\mathbf{x}_i^*)$ at growth locations $\mathbf{x}_i^*$. These values are easily obtained by just choosing vertices of the triangulation used in BIEPACK that approximate these locations. Since BIEPACK returns values of q at each of these vertices, determining $q(\mathbf{x}_i^*)$ amounts to obtaining the solution at the vertex chosen to represent $\mathbf{x}_i^*$.

Our goal is to solve the system $\mathbf{G}(F_{v,i}) = 0$ to determine the unknown fluxes $F_{v,i}$. To solve this system, we pass the subroutine described in Figure 3 to a standard

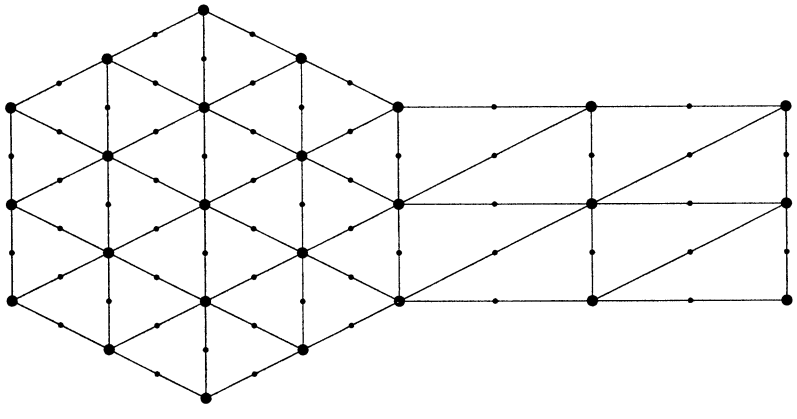

Figure 2. Triangulation of the top and one side of the three-dimensional hexagonal crystal. The midpoints of triangle edges are used, along with triangle vertices, to approximate the integral to second-order accuracy over each triangle. The solution to the potential equation for the mixing ratio is computed at each triangle vertex and midpoint.

Subroutine to compute the non-linear system $\mathbf{G}(F_{v,i})$

$[G_1, G_2] =$ SUBROUTINE $\mathbf{G}(F_{v,1}, F_{v,2})$

1. Obtain two values $\partial q(\mathbf{x}_i)/\partial n$, $i = 1, 2$ from $F_{v,i}$ using

$$\frac{\partial q}{\partial n} = \frac{F_{v,i}}{\rho_{air}\, D_v}, \qquad \mathbf{x} \text{ on face } i,\ i = 1, 2$$

2. Solve the boundary integral equation in (15) subject to the flux conditions given above. This gives us the mixing ratio q on the surface of the crystal.

3. Solve for the temperature field using (13). This gives us the temperature distribution T on the surface of the crystal.

4. The non-linear system is then given by

$$G_i(F_{v,1}, F_{v,2}) \equiv \frac{F_{v,i}}{\rho_{air}\, D_v} - \frac{q_{eq}(T_i^*, p)\, \overline{v}_{th}}{4 D_v}\, \alpha_i^*(\sigma_i^*)\, \sigma_i^*$$

where $\sigma_i^* \equiv \sigma(\mathbf{x}_i^*)$. Note that G_1 and G_2 both depend implicitly upon $F_{v,1}$ and $F_{v,2}$ through q.

Figure 3. Algorithm for determining unknown fluxes $F_{v,i}$.

root-finding routine. The one we chose, HYBRD1 is available through NETLIB and has the advantage that it does not require analytic expressions for the derivatives $\partial G_i/\partial F_{v,j}$ and instead computes numeric approximations to these derivatives. The root-finding routine will return values $F_{v,i}$ that provide consistent boundary conditions for the mixing ratio.

Once we have the proper fluxes $F_{v,i}$, we can determine the velocities of the two faces using (14). With these velocities V_i, we can update the crystal dimensions using

$$d_i^{new} = d_i^{old} + V_i\, \Delta t, \tag{17}$$

where d_i^{new} and d_i^{old} are the new and old dimensions of face i. The time step Δt is chosen to adequately model the dynamics of the growth process. Using the new crystal dimensions, the new fluxes $F_{v,i}$ must be found, the new dimensions are updated, and in this manner the crystal shape evolves.

2.2.3. Accelerated numeric solution method. The root-finding routine evaluates the system described in Figure 3 several times for different trial values of $F_{v,i}$. However, while the root-finding routine is searching for these flux values, the shape of the crystal is not changing, so we can significantly improve the speed of the algorithm by noting that the solution can be written in terms of basis functions $Q_i^\Gamma(\mathbf{x})$ as

$$q(\mathbf{x}) = q_\infty - \frac{1}{\rho_{air}\, D_v} \sum_{k=1}^{2} F_{v,k}\, d_k\, Q_k^\Gamma(\mathbf{x}), \tag{18}$$

where $\Gamma = c/a$ and the basis functions $Q_i^\Gamma(\mathbf{x})$ satisfy the equations

$$\begin{aligned} \nabla^2 Q_i^\Gamma(\mathbf{x}) &= 0, && \mathbf{x} \in \Omega^\Gamma, \\ d_i \frac{\partial Q_i^\Gamma(\mathbf{x})}{\partial n} &= -\delta_{ij}, && \mathbf{x} \text{ on the } j\text{th faces}, \\ Q_i^\Gamma(\mathbf{x}) &= 0, && \mathbf{x} \to \infty, \end{aligned} \tag{19}$$

where $d_1 = c, d_2 = a$, $\delta_{ij} = 1$ if $i = j$ and 0 otherwise, and Ω^Γ is the region of space exterior to a crystal whose dimensions are $d_1 \equiv c = \Gamma$ and $d_2 \equiv a = 1$.

These functions Q_i^Γ can be precomputed using BIEPACK for several Γ values, and values at several possible sets of growth locations can be stored. The root-finding routine then evaluates (18) instead of solving the entire boundary integral equation. For crystal dimensions (c, a) for which c/a lies between precomputed values of Γ, linear or higher-order polynomial interpolation between stored values of the basis function is used.

For simplicity, we consider only three kinds of positions for the ledge sources: the middle of the basal ("c") faces, the middle of the prism ("a") faces, and the corners, where a basal and two prism faces intersect. These are the $\mathbf{x}_i^*$ defined earlier. Figure 4 shows the basis functions $Q_j^\Gamma(\mathbf{x}_i^*), j = 1, 2$, evaluated at each of these ledge source positions. For comparison, we show the basis functions for right circular cylinders of the same aspect ratios, as were derived by *Nelson* [1994]. The curves are quite similar, indicating that the basic features of

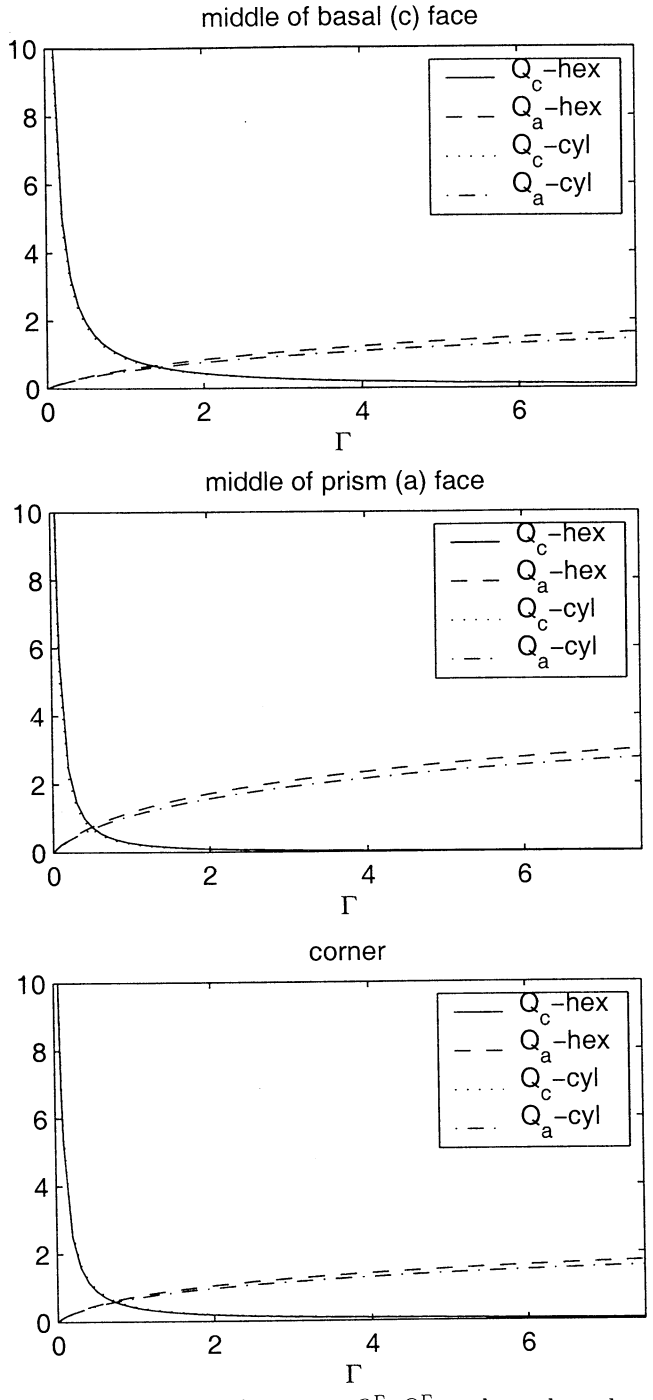

Figure 4. Basis functions Q_c^Γ, Q_a^Γ evaluated at three assumed ledge source positions $\mathbf{x}_i^*$, for the hexagonal crystals and for right circular cylinders of the same aspect ratios Γ.

the vapor diffusion field are not much affected by the faceted nature of the prism faces.

The temperature at ledge sources is also computed using the basis functions. We have

$$T(\mathbf{x}_i^*) = T_\infty - \frac{1}{\kappa} \sum_{k=1}^{2} F_{T,k} d_k Q_k^\Gamma(\mathbf{x}_i^*), \qquad (20)$$

where κ (W/(mK)) is the thermal conductivity of air.

For notational convenience, we drop the superscript Γ on the basis functions from here on.

2.3. Model Limitations

The model as it stands has several limitations.

2.3.1. Size limitation. We are using Laplace's equation to derive fluxes of heat and vapor in the medium, which restricts us to the low Knudsen number regime, in which the crystal is large compared with the vapor mean free path, $\lambda(T,p)$. The mean free path varies from about 0.05 μm at sea level to about 0.4 μm in the upper troposphere, so this condition holds for all tropospheric crystals over a few microns in size.

A more restrictive size limitation stems from the fact that we have not included ventilation in our model to date, so that we focus on crystals smaller than a few 100 μm. Addition of ventilation to the model would involve addition of an advection term to equation (2); in principle, this could be done with minimal increase in complexity of the model.

2.3.2. Shape limitations. As it stands, our crystal growth model is applicable only to regular, faceted hexagonal crystals in which there are only two different linear growth rates, one on each set of equivalent faces. Extension to the full free boundary problem for three-dimensional crystals, where each point of the surface responds to its local environment without the constraint of faceted growth, would be a formidable job requiring many tunable parameters. This problem has been approached for ice only in two dimensions [e.g., *Yokoyama and Kuroda*, 1989]. The limitation to faceted crystals implies a (temperature-dependent) limitation to the supersaturation regimes over which our model applies, as explained in subsequent sections.

2.3.3. Surface kinetics. Within the shape and size limitations mentioned previously, the limitation here is not with our model, but with the lack of knowledge regarding which growth mechanism(s) operate in water ice crystals and some of the physical parameters which control them. These mechanisms and parameters are described in the next section.

3. The Condensation Coefficients

The condensation coefficient α represents the probability that an incident vapor molecule adsorbed on a growing crystal surface will become incorporated into the crystal, and therefore has a value between 0 and 1. The physics of crystal growth lies in the determination of the function relating α to $\sigma(\mathbf{x}_i^*)$, the supersaturation at the crystal surface. Laboratory observations of ice crystal growth at temperatures below about -4°C are usually interpreted in terms of the terrace-ledge-kink (TLK) model [e.g., *Burton et al.*, 1951; *Yokoyama and Kuroda*, 1989; *Kuroda and Lacmann*, 1982] for the surface kinetics at the ice-vapor interface. While the density of vapor molecules impinging on the ice surface at atmospherically relevant temperatures is much higher than that on the crystals to which the TLK model has

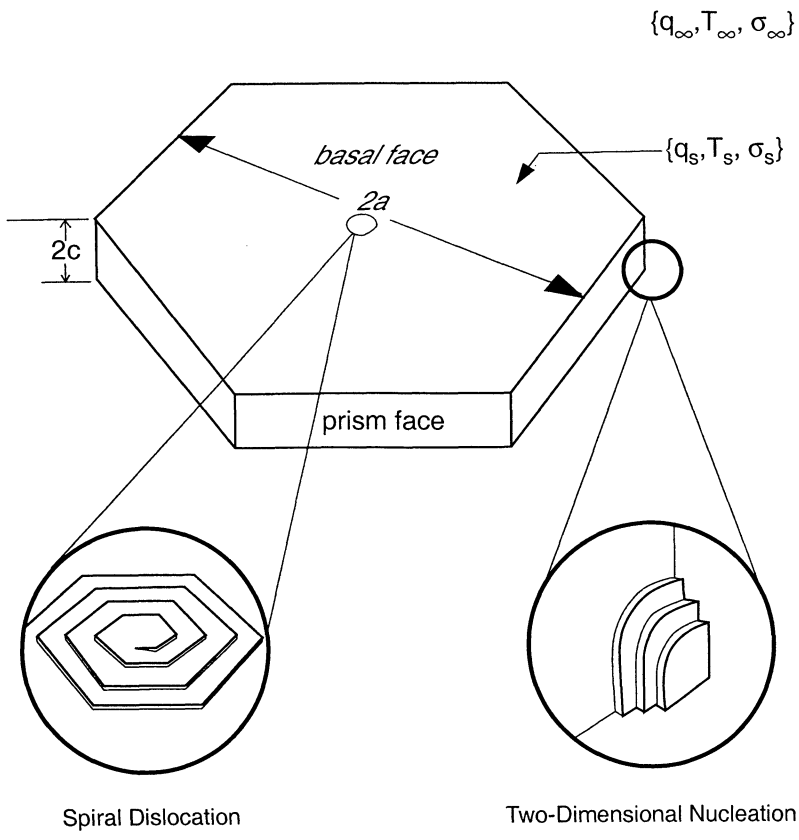

Figure 5. Schematic, crystal in vapor field, showing c, a axes, defining basal, prism faces and the environmental and surface parameters. Insets are schematic representations of microscopic ledge sources for crystal growth, which can occur on any face (see text, section 3).

been applied in general, observations [*Frank*, 1982; *Sei and Gonda*, 1989] suggest certain features of the model also apply to ice.

For our purposes the important feature of the TLK model is that during growth the crystal surface consists of a series of flat areas, or terraces, interrupted at intervals by steps, or ledges, one molecular diameter in height. These are illustrated schematically in Figure 5. Molecules from the vapor land mostly on terraces and diffuse independently on the surface until they encounter ledges, where they become incorporated at kinks, or horizontal "jogs" in the ledge. Ledges advance as a result of incorporation of the new molecules; when a ledge has covered the entire crystal facet, that facet has advanced outward by one molecular diameter. Thus the crystal growth rate is determined by the probability that an incoming molecule will be incorporated into a ledge before it desorbs back to the vapor. This probability increases as the spacing between the ledges decreases. The ledge spacing is controlled by the rate of creation of ledges and their velocity across the surface. The creation rate increases with increasing $\sigma^* = \sigma(\mathbf{x}_i^*)$, and their velocity changes with the local value of σ.

In our model we assume that the ledges are created either by (1) outcropping of screw dislocations, or by (2) two-dimensional nucleation. Screw dislocations can provide a continuous ledge source at any finite supersaturation, and during growth the ledge forms a spiral centered on the dislocation. Two-dimensional nucleation refers to the formation of stable, disk-shaped molecular clusters on the crystal surface, and is a sporadic process occurring only above a certain critical supersaturation. These mechanisms have been observed for a variety of crystals grown in laboratory experiments [e.g., *Kaldis*, 1974]. For simplicity, we assume there is only one ledge generation point on each facet.

3.1. Condensation Coefficients at Ledge Sources

It can be shown [e.g., *Kuroda and Lacmann*, 1982; *Yokoyama and Kuroda*, 1989; *Nelson and Baker*, 1996] that for screw dislocation growth (SDG), the condensation coefficient $\alpha^*(\sigma^*)$ can be represented by the expression

$$\alpha^*(\sigma^*) = (\sigma^*/\sigma_{SD}) \tanh(\sigma_{SD}/\sigma^*), \tag{21}$$

where σ_{SD} is a scaling parameter.

For ledge generation via two-dimensional (2-D) nucleation we can write

$$\alpha^*(\sigma^*) = C_{2D}\sqrt{(\sigma^*)} \exp(-C_{nuc}\sigma^*/\sigma_{cr,2D}), \tag{22}$$

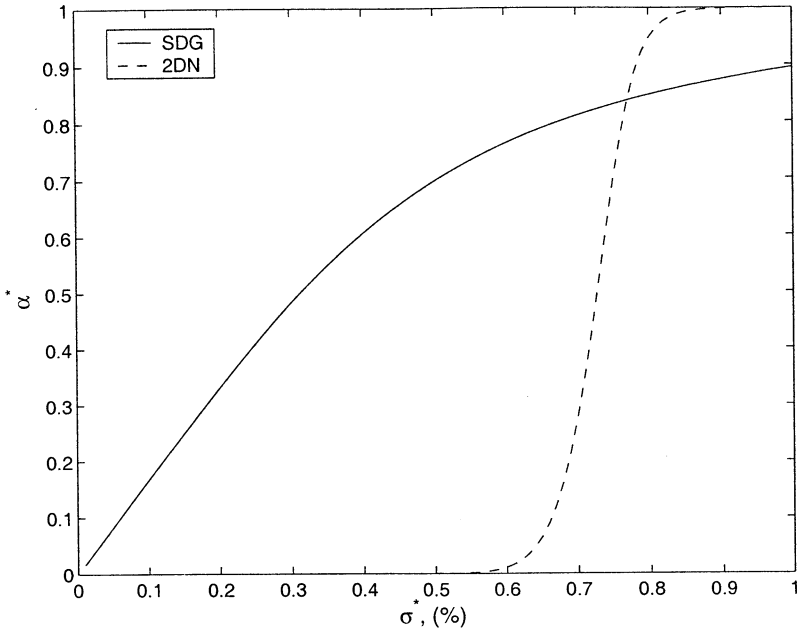

Figure 6. Condensation coefficient $\alpha^*(\sigma^*)$ for cases screw dislocation growth (SDG, solid line) and two-dimensional nucleation (2DN, dotted line), assuming $\sigma_1 = \sigma_{cr,2D} = 0.6\%$

where $\sigma_{cr,2D}$ is the "critical" supersaturation for 2-D nucleation, the primary scaling parameter for this mechanism, and C_{nuc} and C_{2D} are relatively constant factors that depend on temperature, pressure, crystal size, and surface parameters [*Kuroda and Lacmann*, 1982]. Figure 6 shows $\alpha^*(\sigma^*)$ for spiral dislocations (equation (21)) and for 2-D nucleation (equation (22)) with $\sigma_{SD} = \sigma_{cr,2D} = 0.6\%$. From this figure it is clear that in 2-D nucleation there is a threshold to growth at $\sigma^* = \sigma_{cr,2D}$, whereas growth can occur for any positive supersaturation in SDG.

3.2. Spatial Distribution of Condensation Coefficients

Equations (21) and (22) give the functional forms for $\alpha^*(\sigma^*)$, the condensation coefficients at the ledge sources, that is, at $\mathbf{x}_i = \mathbf{x}_i^*$. To define the condensation coefficient α_i at other positions $\mathbf{x_i}$ on the ith crystal face, we recall that in faceted growth $F_{v,i}$ is uniform over each facet. From (8) and (3), we have

$$\alpha^*(\sigma_i^*) = \frac{4F_{v,i}}{\rho_{air} q_{eq}(T_i^*, p)\overline{v}_{th}\sigma_i^*} \tag{23}$$

and

$$\alpha_i \sigma(\mathbf{x}_i) = \alpha^*(\sigma_i^*)\sigma_i^*. \tag{24}$$

Thus we can define a spatially varying function α_i as

$$\alpha_i \equiv \frac{4F_{v,i}}{\rho_{air} q_{eq}(T_i^*, p)\overline{v}_{th}\sigma(\mathbf{x}_i)}, \tag{25}$$

where $\sigma(\mathbf{x}_i)$ is computed from the mixing ratio $q(\mathbf{x}_i)$.

3.3. Surface Kinetics in Crystal Growth Model

We now use these ideas to define several crystal growth scenarios. The ledges created by dislocations that emerge on a facet provide attachment sites for incoming vapor molecules and hence represent vapor sinks on the crystal at all positive supersaturations. However, predicting the probability of dislocations in terms of ambient conditions or nucleation scenario is difficult, if not impossible. It seems unlikely (particularly for large crystals) that the dislocation structure would be so uniform over all six prism faces that symmetric crystals would readily ensue; moreover, laboratory findings [*McKnight and Hallett*, 1978] at −15° and −3°C showed that at those temperatures there were no dislocations on the prism faces. In the absence of dislocations, the ledges can only be generated by 2-D nucleation, so that there is virtually no growth at surface supersaturations below $\sigma_{cr,2D}$.

The presence or absence of dislocations is therefore very important in determining the character of crystal growth, so we have considered several possibilities for the surface structure of the ice crystals in our model.

Let D_n indicate a crystal with emergent dislocations on n sets of faces; that is, D_0 denotes a crystal with no dislocations on any facet (growth can only occur by 2-D nucleation); D_1 denotes a crystal with dislocations present only on one set of faces, prism (D_{1a}) or basal (D_{1c}); and D_2 denotes a crystal with dislocations present on both faces. When dislocations are present, growth occurs by either SDG or 2-D nucleation, depending on which mechanism yields the highest flux. The ledge source location for SDG is always assumed to be at the center of the face, and that for 2-D nucleation is

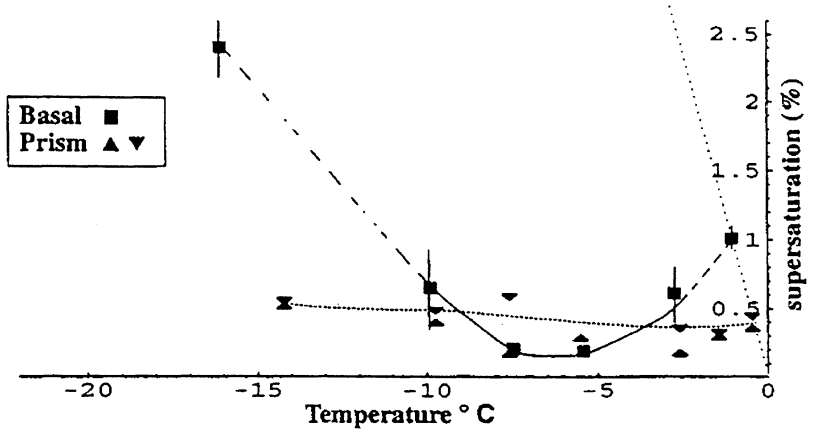

Figure 7. Observed values of $\sigma_{cr,2D}(T)$ on basal and prism faces, reproduced from *Nelson and Knight* [1998]. Error bars for the basal face indicate uncertainty in the supersaturation at which growth started. The solid curve is a fit to the data and is dashed at its ends because slopes are not defined there. The upper limits of the prism face critical supersaturation data (downward pointing triangles) were estimated from observations of equal growth on all prism faces. At 5.5° C an upper limit was not recorded. Lower limits (upward pointing triangles) are the highest supersaturations at which nongrowth of one or more prism faces was observed. The steep dotted line is the ice supersaturation for vapor in equilibrium with supercooled liquid water, and the lower dotted line passes through the prism face data. The effect that growing faces had on reducing the supersaturation on the nongrowing faces was estimated to be less than 10% for the extreme crystal shapes in the experiments. Its effect is not included in the data [*Nelson and Knight*, 1998].

either at the center or corner depending on which has the higher surface supersaturation. Note that as σ_{SD} increases, the crystal facets become more "perfect", or dislocation free, and D_1 and D_2 crystals become equivalent to D_0 crystals.

One of the goals of this paper is to identify the growth mechanisms and, in particular, the apparent role of dislocations, prevalent in different atmospheric cloud regimes. To do this we will compare observations of the crystals that form there with the results of our growth model for different crystal types (D_0, D_1, and D_2).

3.4. The Input Parameters

There are few measurements of the characteristic supersaturation for SDG, σ_{SD}. *Sei and Gonda* [1989] measured values between 0.3% and 3% on the surfaces of ice crystals grown on substrates at temperatures above -30°C. Predicted growth rates are fairly insensitive to the magnitude of σ_{SD}, since α^* is a slowly varying function of this parameter.

Nelson and Knight [1998] obtained empirical values of critical supersaturation for two-dimensional nucleation, $\sigma_{cr,2D}$, for the basal and prism faces of ice crystals grown on the end of a capillary tube at temperatures above -15°C. The faces in contact with the capillary grew at all supersaturations, presumably by SDG, but the free faces often exhibited a sudden onset of growth as the supersaturation was increased. The value at which the onset occurred was taken to be $\sigma_{cr,2D}$. Their results (reprinted here in Figure 7) exhibit a large amount of scatter, but the general pattern is that $\sigma^a_{cr,2D} < \sigma^c_{cr,2D}$ above -4°C and below -9°C, and at temperatures in between, the two values are very close together, with $\sigma^a_{cr,2D}$ perhaps slightly higher than $\sigma^c_{cr,2D}$.

The uncertainty in the measurements, and the limited range of temperatures and humidities over which they were taken, limit the accuracy with which growth rates of crystals can be calculated. However, we are primarily interested in understanding the observed patterns in crystal stability and growth, for which the approximate values of the measured critical values (which are confirmed by independent tests) suffice. Although we use a by-eye fit to the measured average values here for some illustrative figures and calculations, in the main body our major results are presented in terms of the ratio of ambient to surface critical supersaturations, so that they can be applied to new surface parameter measurements as these become available.

A surprising aspect of the laboratory results is the fact that $\sigma_{cr,2D}$ was always so low: less than 1% at temperatures above -10°C, and a maximum of 2.5% at -15°C. Theoretically, the supersaturation scales σ_{SD} and $\sigma_{cr,2D}$ increase with increasing edge free energy γ (J/m), the energy of formation of a step. Calculations of σ_{SD} and $\sigma_{cr,2D}$ from values of γ derived from bond-counting arguments [*Kuroda and Lacmann*, 1982; *Wood*, 1999] yield values $\sigma_{cr,2D} \approx 10 - 100\%$. The difference between theory and observation may be evidence that at temperatures close to the melting point the ice surface is sufficiently disordered that the bond counting arguments are not appropriate. While there exist ice crystal growth models that explicitly describe absorption of vapor into a liquid-like layer [*Fukuta and Lu*, 1994; *Kuroda and Lacmann*, 1982], these involve

parameters and assumptions that have not been measured or tested. We have chosen therefore to estimate the critical supersaturation for 2-D nucleation $\sigma_{cr,2D}(T)$ at $T \geq -15°C$ from the measurements of *Nelson and Knight* [1998].

3.5. Physical Interpretation of Solutions

In the analysis of model results to follow, it is convenient to conceptualize some of the important equations from the previous sections. From equation (8), we see the flux to any point on the ith face increases with supersaturation at the ledge source location on that face:

$$F_{v,i} \propto \alpha^*{}_i \sigma_i^*. \tag{26}$$

Another relationship between $F_{v,i}$ and σ_i^* comes from (18), which shows that the vapor concentration at the surface of a growing crystal is less than that in the ambient air because the growing crystal faces serve as vapor sinks. For the purposes of qualitative analysis we can make the approximation that $q_{eq}(T_\infty, p) \simeq q_{eq}(T(\mathbf{x}), p)$, so equation (18) can be written

$$\sigma_i^* = \sigma_\infty - \frac{1}{\rho_{air}\, D_v\, q_{eq}(T_\infty, p)} \sum_{k=1}^{2} F_{v,k} d_k Q_k(\mathbf{x}_i^*) \equiv \sigma_\infty - \sum_{k=1}^{2} \alpha_k^* \sigma_k^*\, d_k'\, Q_k(\mathbf{x}_i^*), \tag{27}$$

where $d' \equiv d/\lambda$ and λ is the vapor mean free path: $\lambda \approx D_v/\bar{v}_{th}$. The product $\alpha_1^* \sigma_{SD}^* d_1' Q_1(\mathbf{x}_2^*)$, for example, represents the loss of vapor at the ledge sources on the prism faces due to the fluxes to the basal faces; according to equation (27), σ_i^* decreases with $F_{v,i}$ because of the vapor sink on the ith surface during its growth.

Our model solves the crystal growth problem by finding the values of σ_i^* that simultaneously satisfy (26) and (27).

4. Model Results

We have applied our numerical model to the investigation of the link between surface parameters and macroscopic crystal properties over a range of parameter values relevant to atmospheric clouds. We discuss our results in this and the next section of the paper.

4.1. Instantaneous Mass Growth Rates: Comparisons to Other Models

The rate of mass growth of a crystal ($\dot{M}$) is usually approximated in atmospheric work by use of the so-called capacitance model in which the crystals are assumed to be ellipsoids of revolution or spheres. In these models the surface kinetic processes of crystal growth are not treated, and the supersaturation at the surface of the particle is assumed to be zero. According to the capacitance model, in the low Knudsen number ($Kn = \lambda/d$) regime, the rate of growth of a solid ellipsoid of revolution of major and minor axes c_{cap}, a_{cap} is

$$\dot{M}|_{cap} = \frac{D_v \rho_{air} q_{eq}(T_\infty, p) \sigma_\infty 4\pi C(a_{cap}, c_{cap})}{1 + Z(T,p)}, \tag{28}$$

where $C(a_{cap}, c_{cap})$ is the capacitance of the ellipsoid and $Z(T,p)$ is a measure of the thermal impedance to growth:

$$Z(T,p) \equiv \frac{D_v L_{sub} \rho_{air} q_{eq,\infty}}{\kappa T} \left(\frac{L_{sub}}{R_v T} - 1 \right), \tag{29}$$

where R_v is the specific gas constant for water vapor [*Pruppacher and Klett*, 1997]. The capacitance of a sphere is its radius, so the mass growth rate of a sphere of radius r_{eq} in the low Kn regime is

$$\dot{M}|_{sphere} = \frac{D_v \rho_{air} q_{eq}(T_\infty, p) \sigma_\infty 4\pi r_{eq}}{1 + Z(T,p)}, \tag{30}$$

Our hexagonal crystal model calculates the linear growth rates $\dot{a}$ and $\dot{c}$ of each crystal face, so the total mass growth rate for a solid hexagonal prism is given by

$$\dot{M}|_{hex} = \frac{12}{\sqrt{3}} \rho_{ice} a (2c\dot{a} + a\dot{c}). \tag{31}$$

The two main differences between our model and the capacitance model lie in their treatments of crystal shape and the microphysics of crystal growth. We calculate the growth of regular hexagonal prisms instead of ellipsoids or spheres and relate the evolution of particle shape to surface parameters that can in principle be measured. The capacitance model can be used to simulate crystals with different shapes and aspect ratios, but it cannot predict what those shapes will be. Also, in the capacitance and sphere models the diffusive flux to a crystal is proportional to σ_∞; the surface supersaturation is zero everywhere. In reality, σ_i^* must be greater than zero on the surface in order to drive the surface kinetic processes of crystal growth [*Kuroda*, 1984]. In our model the flux to the ith facet is proportional to $\sigma_\infty - \sigma_i^*$, where $\sigma_i^* > 0$, as determined by the solution to equations (26) and (27). For a given crystal shape, the flux of vapor to the crystal predicted by our model can therefore be much smaller than that given by the capacitance or sphere models.

In order to observe the effects of these differences, we have compared the instantaneous mass growth rates predicted by each of four crystal growth models: (1) HEX-D_2: our hexagonal crystal model for type D_2 crystals (those with dislocations on all basal and prism faces); (2) HEX-D_0: our hexagonal crystal model for type D_0 crystals (those with no dislocations), where we assumed $\sigma_{cr,2D}(c,a) = (0.6\%, 0.5\%)$ [*Nelson and Knight*, 1998], and $\sigma_{SD} = \sigma_{cr,2D}$ on each face; (3) CAP-ell: the capacitance model (equation (28)) for an equal volume ellipsoid of the same aspect ratio; and (4) CAP-sph: the sphere model (equation (30)) for a sphere of

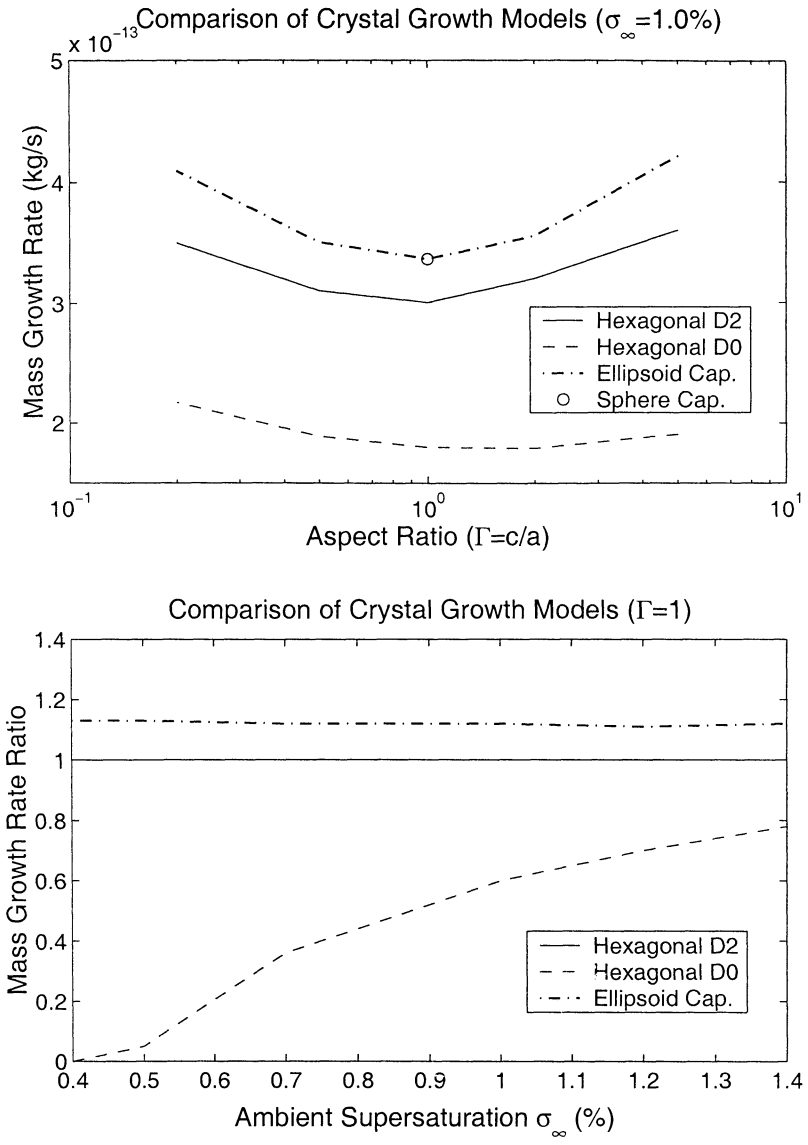

Figure 8. Comparison of mass growth rates predicted by our hexagonal crystal model for D_2 crystals (solid lines) and D_0 crystals (dashed lines), and by the capacitance model for equivalent volume ellipsoids (dotted lines) and spheres (circle). The upper plot shows the effect of changing the aspect ratio while keeping the supersaturation constant. The lower plot shows the effect of changing the supersaturation for isometric crystals. The ambient conditions used for these calculations were $T = -10°C$, $p = 500$ mbar, and the spherical crystal radius was 59 μm. We assumed $\sigma_{cr,2D}(c,a) = (0.58\%, 0.55\%)$ [*Nelson and Knight*, 1998], and $\sigma_{SD} = \sigma_{cr,2D}$ on each face.

the same volume. The resulting values for each model are shown in Figure 8, plotted as functions of aspect ratio and ambient supersaturation. To better isolate the effects of changing these parameters, the same crystal mass was used for each model calculation (8×10^{-10} kg).

4.1.1. Effects of crystal shape. The effects of using different crystal shapes on the model-calculated mass growth rates are best seen (in Figure 8) in the HEX-D_2 and capacitance models because the capacitance model does not include surface kinetics and, although our model does, its effects are small for D_2 crystals for the parameter values used here. The reason for the observed variation with aspect ratio is that the mass growth rate is proportional to the crystal capacitance, related in general to the longest linear dimension of the crystal. For both ellipsoids and hexagonal prisms the capacitance (or effective capacitance) is minimum for isometric crystals and increases by about 20% for both models as $\Gamma \to 0.2$ and $\Gamma \to 5$. Thus (1) $\dot{M}$ is minimum for isometric crystals for both models and (2) the ratio of growth rates predicted by the HEX-D_2 and CAP-ell models is almost a constant independent of Γ. This constant is approximately equal to the ratio $a_{cap}/a = 1.18$ for an equivalent volume ellipsoid and hexagonal prism. Therefore had we used the same crys-

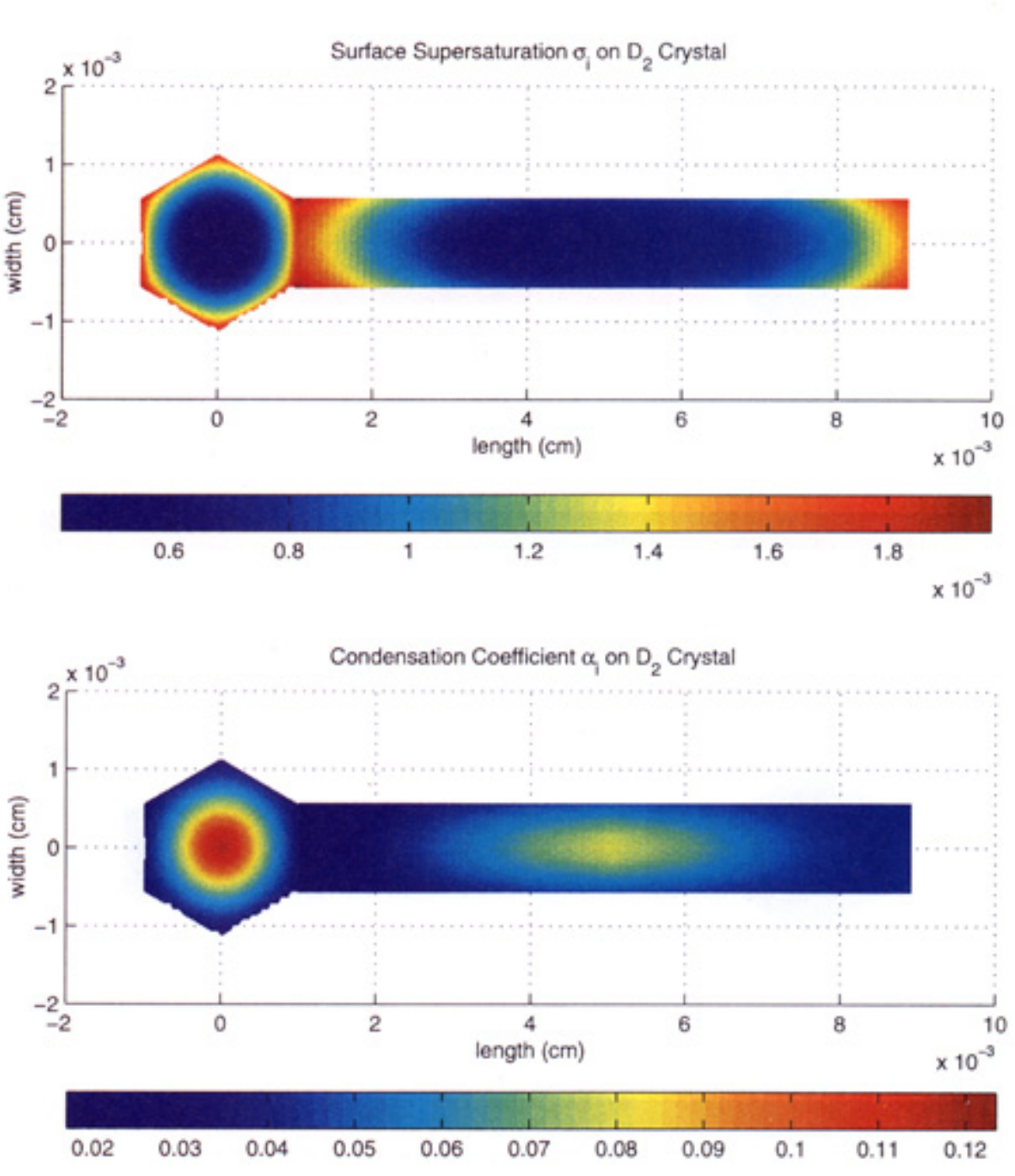

Plate 1. Model-calculated distributions of surface supersaturation and condensation coefficient for a D_2 crystal ($a = 10$ μm, $\Gamma = 4$) growing at $T = -9°$C, $p = 600$ mbar, and $\sigma_\infty = 0.7\%$. The shape of the crystal is a three-dimensional hexagonal prism, but contours are shown on only one basal face (hexagon) and one prism face (rectangle). For this calculation we have assumed values for the critical supersaturation read from Figure 7: $\sigma^c_{cr,2D} = 0.4\%$ and $\sigma^a_{cr,2D} = 0.5\%$. The calculated linear growth rates are $\dot{c} = 0.019\mu$m/s and $\dot{a} = 0.012\mu$m/s, giving a mass growth rate of $\dot{M} = 7.2 \times 10^{-11}$ g/s.

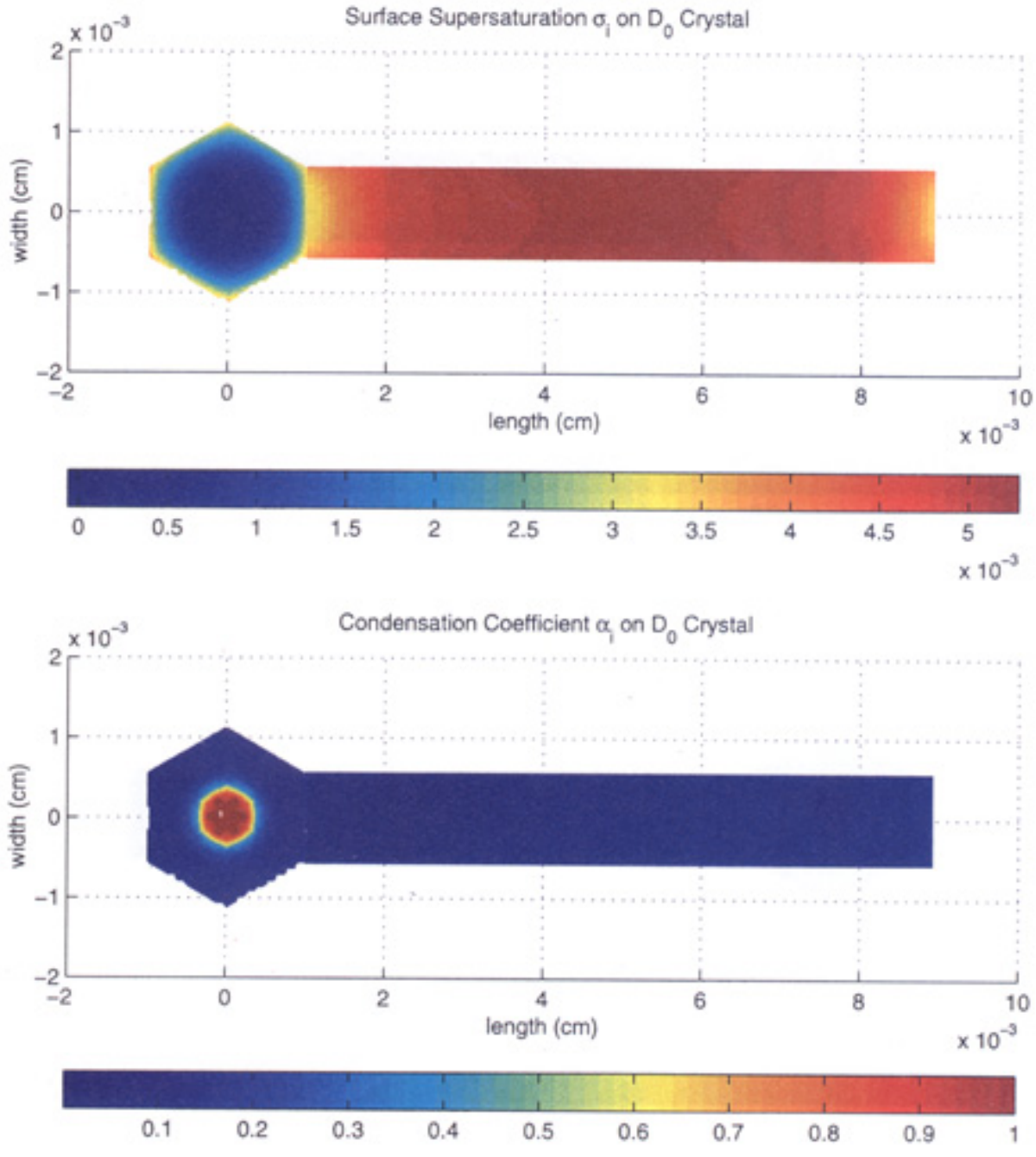

Plate 2. Model-calculated distributions of surface supersaturation and condensation coefficient for a D_0 crystal ($a = 10$ μm, $\Gamma = 4$) growing under the same conditions as in the previous plate ($T = -9°$C, $p = 600$ mbar, and $\sigma_\infty = 0.7\%$). The calculated linear growth rates in this case are quite anisometric with $\dot{c} = 0.035\mu$m/s and $\dot{a} = 0.002\mu$m/s, giving a mass growth rate of $\dot{M} = 3.1 \times 10^{-11}$ g/s.

tal dimensions rather than the same crystal mass in the HEX-D_2 and CAP-ell models, we would have obtained nearly identical mass growth rates for each aspect ratio.

4.1.2. Effects of surface kinetics. In the HEX-D_0 model, dislocations are absent so that growth can occur only by 2-D nucleation. At low σ_∞, growth is highly hindered. When the ratio $\sigma_\infty/\sigma_{cr,2D} \leq 1$, the growth rate is nearly zero, and for $\sigma_\infty/\sigma_{cr,2D} \simeq 2.5$ it is still reduced by about 20% relative to model HEX-D_2. (At higher values of $\sigma_\infty/\sigma_{cr,2D}$ faceted growth becomes unstable for D_0 crystals, so that we cannot calculate growth rates beyond this point. A detailed discussion of this "stability limit" will be given in section 4.3).

4.1.3. Summary. In summary, for $0.2 \leq \Gamma \leq 5.0$, mass growth rates computed from the capacitance and the sphere models for equal volume shapes are within $10 - 20\%$ of those calculated by our flat-faced hexagonal crystal model if dislocations are plentiful, that is, for D_2 crystals, low σ_{SD}. Much larger errors are possible if surface kinetics are neglected in cases where dislocations are not present and the ambient supersaturation is less than a few times $\sigma_{cr,2D}$. The values of $\sigma_{cr,2D}$ measured by *Nelson and Knight* [1998] for $T \geq -15°C$ are $\simeq 1\%$, but because liquid droplets are likely to also be present in clouds at these temperatures, and because in vapor saturated with respect to liquid water at temperature T (°C), the supersaturation with respect to ice is approximately $|T|\%$, it is usually the case that $\sigma_\infty \gg \sigma_{cr,2D}$, so that crystal surface kinetics will only affect shape and not growth rates. However at lower temperatures such as in cirrus clouds, there is evidence (discussed in section 5) that $\sigma_{cr,2D}$ is much higher ($\geq 10\%$), so that surface kinetics could limit growth rates over a much larger range of atmospheric conditions, and would therefore be a more important model process to take into account.

4.2. Surface Distributions of σ and α

Our model can be used to calculate the supersaturation and condensation coefficient at each point on the surface of a hexagonal ice crystal. Examination of several examples illustrates the important features of these distributions and of their dependence on crystal surface structure.

4.2.1. Type D_2 crystal. Plate 1 shows the calculated distribution of supersaturation on the basal and prism faces of a columnar D_2 crystal at $T = -9°C$, calculated by assuming values of the critical supersaturations in the middle of the range measured by *Nelson and Knight* [1998] at this temperature. In this case the surface supersaturation is highest at the corners of each face and decreases toward the center, and both faces are growing by SDG. Note that the maximum value of σ is almost equal to $\sigma^c_{cr,2D} = 0.4\%$, the lower of the two critical supersaturations; any further increase in σ_∞ would make 2-D nucleation at the corner the dominant growth mechanism.

Also shown in Plate 1 is the corresponding spatial distribution of α computed from equation (25). On both faces the condensation coefficient increases toward the center to compensate for the decreasing supersaturation and maintain a uniform growth rate. Physically, this occurs because the steps nucleated at the center speed up as they move into regions of higher supersaturation, thus decreasing the slope or density of ledges and making it less probable for adsorbed molecules to become incorporated. Note, however, that α does not approach 1 anywhere on the crystal. Both faces are growing at approximately the same rate (0.04 μm/s), so this crystal would tend to become more isometric under constant conditions.

4.2.2. Type D_0 crystal. Plate 2 shows the surface distributions of σ and α for a D_0 crystal of the same shape as in the previous case, and growing under the same conditions. It is a general result of our model that for corner ledge nucleation ($\mathbf{x}^*_i = x_{\text{corner}}$) the supersaturation is equal to the lower of the two critical supersaturations for 2-D nucleation on each face ($\sigma(\mathbf{x}^*_i) \approx \sigma^{low}_{cr,2D} \equiv \min[\sigma^c_{cr,2D}, \sigma^a_{cr,2D}]$). The supersaturation on the basal face is once again greatest at the corners of the crystal where it is maintained at or near $\sigma^{low}_{cr,2D} = \sigma^c_{cr,2D} = 0.4\%$. On the prism faces, however, σ is greatest at the center. The value at the corners is too low for 2-D nucleation on the prism face at this temperature, but σ increases toward the center to values close to $\sigma^a_{cr,2D} = 0.5\%$. Two-dimensional nucleation growth thus occurs but at a much slower rate than on the basal faces.

The surface distribution of the condensation coefficient shows that α reaches its maximum value of 1 near the center of the basal face, indicating that uniform growth could not be maintained for any further increase in the ambient supersaturation. In other words, $\sigma_\infty = 0.7\%$ represents the stability limit for faceted growth of D_0 crystals (of this size and shape) at this temperature, in contrast to the D_2 crystal case described above which had all faces growing uniformly at $\sigma_\infty = 1.5\%$. General results regarding the stability limit will be discussed in section 4.3.

Although the figures shown here were calculated using a high-resolution triangulation with 770 vertices, the lower resolution (194 vertices) shown in Figure 2 gives nearly identical results.

For most applications, we do not need to know the full distribution of σ and α on the crystal surface, and are only interested in the linear growth rates of each face (which together give the total or mass growth rate) and whether or not uniform growth of each face is stable. This information can be obtained using the accelerated solution method described in section 2.2.3, in which σ and α are calculated only at the corner and center of each face.

4.3. Limits to Stable (Flat Faced) Growth

From observations of vapor-grown ice crystals in the atmosphere and in the laboratory, it is well known that compact faceted shapes are usually found at low su-

persaturations while hollowed or dendritic shapes are found at high supersaturations (see Figure 1). The empirical boundary between these two regimes seems to depend on temperature but is not well characterized. The shape of ice crystals plays an important role in determining their radiative properties, fall speeds, and collision/collection efficiencies, so it is valuable to have a way of predicting this shape transition in cloud models. Using our crystal growth model, we can calculate the highest ambient supersaturation for which facets can remain flat, σ_∞^{hol}, in terms of given values for the critical supersaturation for 2-D nucleation, $\sigma_{cr,2D}$, on each face. As better measurements of $\sigma_{cr,2D}$ become available, our model predictions can be more confidently translated into actual atmospheric supersaturation values.

Since the flux to any point $\mathbf{x}$ on a face is proportional to the product $\alpha(\mathbf{x})\sigma(\mathbf{x})$, growing crystals can maintain macroscopically flat faces only as long as this product is constant across each face, that is, as long as

$$\alpha(\mathbf{x})\sigma(\mathbf{x}) = \alpha^*\sigma^* \tag{32}$$

for all $\mathbf{x}$ on the face (see equation (24)). For the faster growing faces, which are the first ones to hollow, or become concave, the surface supersaturation is highest at the corners and lowest at the center. If the ledge source is at the center of the crystal face, then ledges speed up as they move into regions of higher $\sigma(\mathbf{x})$, spread out, and decrease the local α. There is no limit to how much α can decrease, so this situation is always stable. If the ledge source is the corner (or the corner source becomes dominant), then ledges slow down and "bunch up" as they approach the center, so that $\alpha(\mathbf{x})$ increases toward the center (see Plate 2) and a uniform growth rate can still be maintained, but only up to a point. This equality breaks down when $\alpha(\mathbf{x})$ reaches its maximum value of unity. When the growth rate at the center

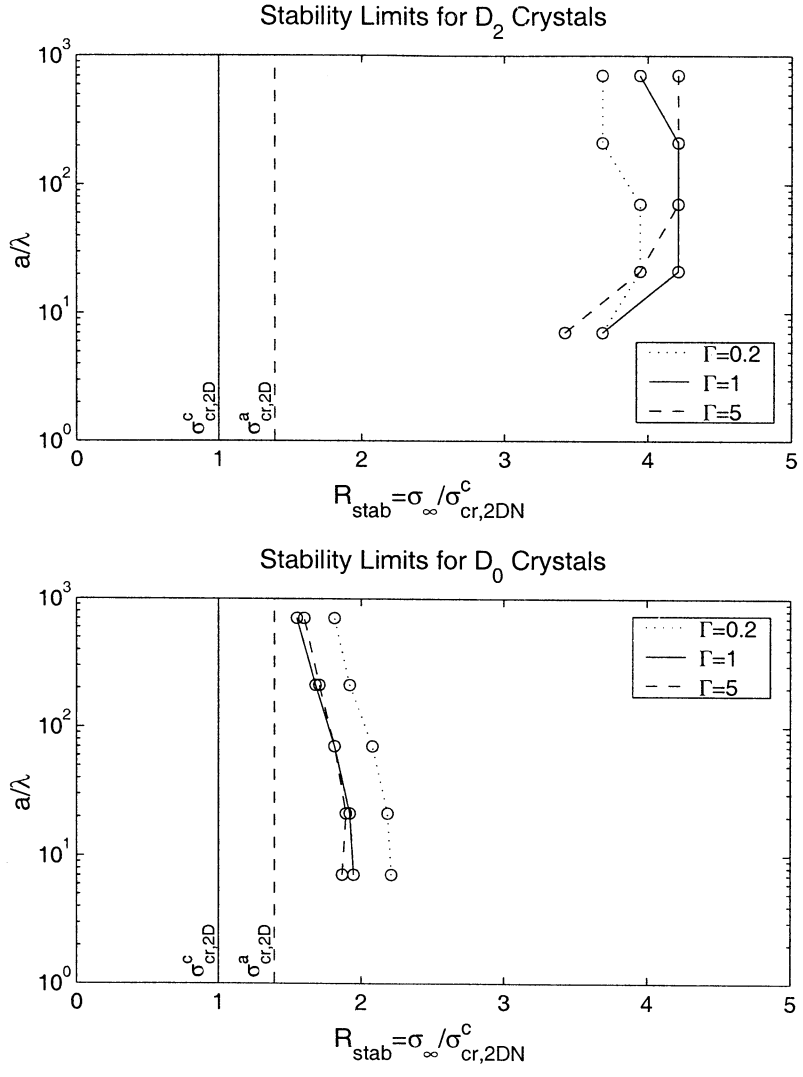

Figure 9. Calculated values (open circles) for the critical ambient supersaturation σ_∞^{hol} at which uniform growth of the basal faces breaks down and hollowing begins for (top) D_2 crystals and (bottom) D_0 crystals of varying size and aspect ratio. Crystal sizes are a =1, 3, 10, 30, and 100 μm plotted in units of the vapor mean free path λ. $T = -9°$ C, p = 600 mbar. Growth on the hollowing basal faces is by 2-D nucleation.

of the face can no longer keep up with that of the outer portions, the face begins to hollow. Thus stable growth is possible only for [*Nelson*, 1994]

$$\frac{\alpha^*\sigma^*}{\sigma_{(\mathbf{x}_{mid})}} = \alpha(\mathbf{x}_{mid}) \leq 1. \quad (33)$$

We have noted that in general, 2-D nucleation growth maintains the corner supersaturation at a value close to $\sigma^{low}_{cr,2D} = \min\left[\sigma^a_{cr,2D}, \sigma^c_{cr,2D}\right])$, independent of σ_∞. Therefore as σ_∞ increases, the normal gradient $\partial\sigma/\partial n \simeq (\sigma_\infty - \sigma^*)/d$ must increase. This in turn increases the flux $F_v \propto \alpha^*\sigma^*$ (according to equation (26)), as well as the gradient in supersaturation parallel to the face (reducing $\sigma(\mathbf{x}_{mid})$), so that condition (33) is met. Eventually, at some limiting value $\sigma_\infty \equiv \sigma^{hol}_\infty$ the condition (33) can no longer be satisfied, and the crystal face hollows.

We have calculated the ratio $\sigma^{hol}_\infty/\sigma^{low}_{cr,2D} \equiv R_{stab}$ for a range of crystal and ambient parameters. Our results, some of which are plotted in Figure 9, show that $2 \leq R_{stab} \leq 5$ over the range of values we examined, and within this range R_{stab} depends to some extent on crystal type. For D_0 crystals, $R_{stab} \simeq 2$ to 3. For D_2 crystals, R_{stab} depends on σ_{SD} on the hollowing face; $R_{stab} \simeq 4$ to 5 for $\sigma_{SD} = \sigma^{low}_{cr,2D}$. As σ_{SD} increases, the D_2 crystals effectively become D_0 crystals, and R_{stab} decreases. The value of R_{stab} is not very sensitive to either the crystal aspect ratio, or perhaps more surprisingly, its size.

The results for R_{stab} can be roughly summarized by the following simple arguments:

1. R_{stab} is nearly independent of crystal size. As we have seen, the corner supersaturation is fixed at all crystal sizes; $\sigma(\text{corner}) \approx \sigma^{\text{low}}_{\text{cr,2D}}$. If the gradient in σ parallel to the crystal surface were independent of crystal size, then an increase in crystal size would result in lower values of $\sigma_{s,mid}$, and the hollowing condition would be approached sooner for larger crystals. At very large sizes this, in fact, is the case. However, the gradient parallel to the face is approximately proportional to the gradient perpendicular to the face (or flux) over the range of sizes we examined. Since the flux *decreases* with crystal size (at constant σ_∞), the parallel gradient of σ decreases with increasing crystal size, and $\sigma_{s,mid}$ remains fairly constant over a large size range.

2. The value of R_{stab} is between 2 and 5. The values obtained for R_{stab} can be qualitatively understood in terms of equation (27). We designate the faces with the lower of the two critical supersaturation values "low", and the other faces we designate "hi". As σ_∞ increases, a given crystal starts to hollow first on the "low" faces, so that we can write

$$\begin{aligned} R_{stab} &\equiv \sigma_\infty/\sigma^{low}_{cr,2D} \\ &\approx 1 + \alpha^*_{low} d'_{low} Q_{low} + \alpha^*_{hi} d'_{hi} Q_{hi} \left(\frac{\sigma^*_{hi}}{\sigma^{low}_{cr,2D}}\right). \end{aligned} \quad (34)$$

The term $\alpha^*_j d'_j Q_j$ is the ratio of the diffusive and surface kinetic resistances to growth on the jth faces. Diffusion between the crystal and the environment tends to favor growth at the corners because corners penetrate farther into the vapor or temperature gradient, a tendency counteracted at low supersaturation by the spatial variation in condensation coefficient (equation (25)). On a nearly hollowing face the ledge sources are at the corners. The face can only remain flat as long as the ratio of diffusive to kinetic resistance remains less than or equal to 1, so the minimum value of R_{stab} is approximately 2. The last term in equation (34) represents the reduction of supersaturation on the hollowing faces due to the vapor sink on the nonhollowing, "hi" faces. This term is largest on D_2 crystals, when growth on the nonhollowing face occurs via SDG.

4.4. Steady State Growth Shapes

In this section we calculate the "steady state" growth shape that develops in vapor growth under constant environmental conditions for comparison with published habit diagrams [*Nakaya et al.*, 1958; *Auer and Veal*, 1970; *Chen and Lamb*, 1994] based on laboratory and field data. Observed aspect ratios of small (< 100 μm) ice crystals typically range between 0.2 and 5.0 over the 0° to -30°C temperature range, and the alternations between planar and columnar habits are consistently seen at around -4°, -10°, and -22°C.

For comparison with these data, we have calculated the aspect ratio of initially isometric crystals after 10 minutes of growth, for a range of values T_∞ and σ_∞. The aspect ratio continues to change as the crystal grows and does not achieve a true steady state, but the rate of change decreases significantly after a few minutes of growth for the conditions used here. Our results for three different assumptions regarding crystal surface properties are shown in Figure 10. Also indicated on these plots are the maximum ambient supersaturations at which uniform growth is stable, as discussed in the previous section.

For each crystal type we see the observed transitions between planar ($\Gamma < 1$) and columnar ($\Gamma > 1$) crystals at around -3°C and -10°C for all crystal growth types, a result of the variations with temperature in observed $\sigma_{cr,2D}$. The transitions become more abrupt as σ_∞ increases and as the growth mode changes from SDG with low σ_{SD} to SDG with high σ_{SD} to 2-D nucleation, that is, as dislocations become less important. For $\sigma_\infty > \sigma^{hol}_\infty$ the crystals hollow, so the predicted aspect ratios cannot be analyzed quantitatively in this regime.

The figures show that as long as dislocations are present on every face (D_2 crystals) and σ_{SD} is low, only fairly isometric crystals remain unhollowed, but as SDG growth becomes less important (σ_{SD} increases), more anisometric crystals can remain faceted if the ambient supersaturation remains below the stability limit. For D_0 crystals we find a wider range of aspect ratios in

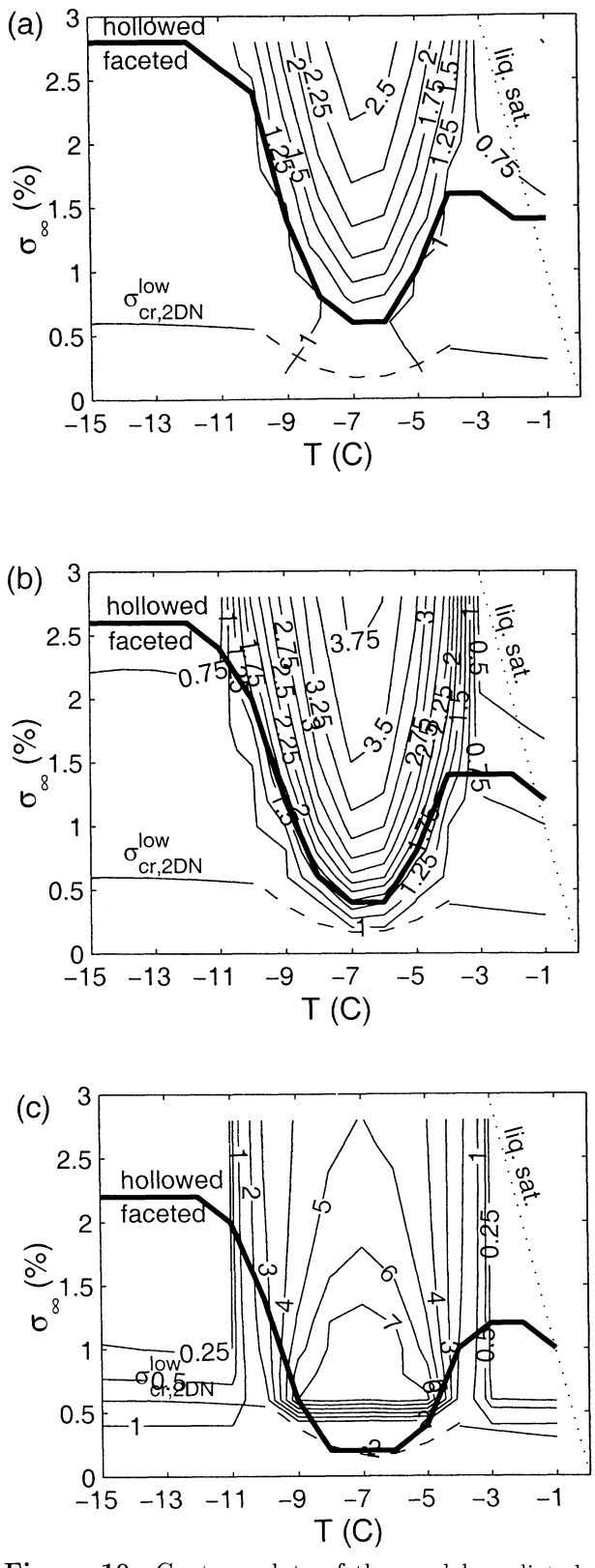

Figure 10. Contour plots of the model-predicted aspect ratio of initially isometric crystals after 10 min of growth under constant conditions for (a) D_2 crystals with $\sigma_{SD} = \sigma_{cr,2D}$, (b) D_2 crystals with $\sigma_{SD} = 10\%$, and (c) D_0 crystals. *Nelson and Knight*'s [1998] measurements were used for $\sigma_{cr,2D}$. Thick line denotes maximum supersaturations σ_∞^{hol} at which uniform growth is stable.

the faceted regime than for the other types: from less than 0.25 to greater than 3, and an indication of much higher values for hollowed crystals. Although 2-D nucleation growth explains the overall habit variation with temperature, the fact that observed aspect ratios are usually more moderate at temperatures above −30°C suggests that dislocations also play a role in the growth of atmospheric ice crystals.

5. Interpretation of Field Observations

The stability criteria we have derived depend on the critical supersaturation values of each crystal facet. In the temperature regime for which we have data on surface parameters, we can infer the crystal growth processes from observed crystal shapes and our stability plots. At lower temperatures we infer values of $\sigma_{cr,2D}$ based on field observations of faceted, hexagonal crystals at known temperatures and supersaturations.

5.1. Mixed Phase Clouds

At the warm temperatures and high ice supersaturations (due to the presence of liquid water) in mixed phase clouds, σ_∞ usually exceeds our predicted stability limit of $5\sigma_{cr,2D}$ on both faces, and indeed most crystals have at least some hollowed or dendritic faces. The basic habit changes with temperature can be explained by 2-D nucleation growth on at least one set of faces together with temperature-dependent values of $\sigma_{cr,2D}$ [*Nelson and Knight*, 1998]. Based on our results in the previous section, the presence of dislocations on the nonhollowing faces would probably produce crystals with more moderate aspect ratios than if they were absent, so that comparisons of model predictions with observed aspect ratios [e.g., *Auer and Veal*, 1970] could potentially be used to infer dislocation occurrence frequencies for ice crystals in warm, mixed phase clouds. However, because our model is limited to faceted crystals, we cannot yet make the quantitative predictions required for this comparison.

5.2. Arctic Cirrus Data

Korolev et al. [1999] presented in situ pictures of crystals in Arctic cirrus clouds at temperatures ranging from -11° to -36°C. These show that fewer than 10% of the crystals larger than 40 μm (their shape resolution limit) have compact shapes with flat facets and sharp corners and that most are irregularly shaped polycrystals or rounded (presumably sublimating) crystals.

There are several possible reasons for the rarity of large pristine crystals. Nucleation at low temperatures may produce polycrystalline ice [*Pruppacher and Klett*, 1997], or these irregular crystals could be the result of coagulation of smaller pristine crystals [*Jensen et al.*, 1994a]. Alternatively, the irregular shapes could be due to the increasing effects of ventilation on larger particles as they fall.

Most of the columns were found at temperatures below -22°C, and most of the thin plates were found at temperatures ≥ -22°C, as observed by others [see *Kobayashi*, 1965; *Chen and Lamb*, 1994]. However, most of the so-called thick unhollowed plates were also found at these lower temperatures where columns might be expected. These are the smallest crystals shown by *Korolev et al.* [1999], and it may be they are the youngest, having formed from frozen droplets without traveling far from their formation location. Freezing at low temperatures could lead to the creation of many dislocations, and therefore the growth may occur via SDG, explaining the fairly isometric shapes. We suggest these are D_2 crystals.

The measured supersaturations corresponding to these crystals range from a few per cent at the higher temperatures to around 40% at the lower temperatures. Some of the crystals are quite anisometric, with $\Gamma \approx 5$, without visible hollowing. Given the high ambient supersaturations, the fact that growth on some facets is severely hindered without hollowing implies (Figure 9) that on those facets the values of $\sigma_{cr,2D}$ are comparable to the high theoretical values calculated by *Kuroda and Lacmann* [1982], *Wood* [1999], and others. If this is the case, these are probably D_1 crystals.

5.3. Antarctic "Diamond Dust"

Diamond dust refers to ice crystals which are often observed to precipitate from relatively clear skies in Antarctica. A large fraction of these crystals have pristine faceted shapes. *Kikuchi and Hogan* [1979] collected many of these crystals on Formvar-coated slides, and using a microscope observed a wide variety of shapes, including hexagonal columns and plates as well as trapezoidal, triangular, and rhomboidal crystals. The dominant shape was columnar with an average aspect ratio ranging from 2.5 to 5.5, although many crystals with $\Gamma \geq 10$ were also seen. S. Warren (personal communication, 1999) has also observed long, thin, unhollowed columnar crystals in Antarctica simultaneously with small, nearly isometric, unhollowed crystals. Inferred air temperatures during Kikuchi and Hogan's observations were around -37° to -35°C, and σ_∞ was typically $\sim 30 - 40\%$ in the lowest 3 km of the atmosphere. Columns are the expected shapes at these temperatures [*Kobayashi*, 1965], but it is at first surprising to find that most crystals are not hollowed and that some have such large aspect ratios while others from the same locations are nearly isometric.

The Arctic and Antarctic observations suggest that at low temperatures (1) the high aspect ratio crystals are D_1 crystals with dislocations only on the basal faces, while (2) the small isometric crystals are D_2 crystals with dislocations on both prism and basal faces, and (3) the values of $\sigma_{cr,2D}$ are much higher than have been measured for $T \geq -15$°C. The extreme aspect ratios are reproduced by our model if we assume that the critical supersaturation values are of the order of 10% and that the values of σ_{SD} are consistent with those measured in the laboratory [*Sei and Gonda*, 1989].

In order to explore possible explanations for the trigonal [*Yamashita*, 1973] and quadrilateral forms, we have investigated the supersaturation distributions on D_{1a} crystals with dislocations on only some of the prism faces. An obvious explanation for trigonal shapes would be that these crystals had dislocations on every other prism face and, if $\sigma_\infty \leq \sigma^a_{cr,2D}$, these faces would grow out of existence leaving only the three nongrowing prism faces. Likewise, quadrilateral plates could be D_{1a} crystals with dislocations only on two opposite prism faces. However, nonsymmetric dislocation distributions can also lead to symmetric crystals. Our model calculations show that lower supersaturations occur on the prism faces adjacent to the face(s) on which the vapor sink is greater, and vice versa. Also, subsequent small distortions in crystal shape do not appear to modify the supersaturation distributions greatly. This suggests, for example, that having a dislocation on just one prism face would suppress growth on the adjacent faces, which would in turn enhance growth on the faces adjacent to those, which would suppress growth on the face opposite the dislocation, producing a trigonal crystal.

6. Habit and Stability Diagram ($-30° < T < 0$°C)

From the interpretations of observed crystal shapes given above, we have constructed plausible functions $\sigma^c_{cr,2D}(T)$ and $\sigma^a_{cr,2D}(T)$ for $-30° < T < -15$°C which merge into the values measured by *Nelson and Knight* [1998] at higher temperatures. Based on these functions we can extend our calculations of the stability limits for D_2 and D_0 crystals (as in Figures 9 and 10) to lower temperatures. The results are shown in Plate 3. While the calculations below -15°C are based on conjecture, they illustrate several important points. Faceted crystals are likely to be stable at much higher σ_∞ at low temperatures than they are at higher temperatures, potentially even in the presence of supercooled liquid droplets. There is also a much wider range of supersaturations below $\sigma_{cr,2D}$, making it more likely that models that do not take into account crystal surface kinetics will be inaccurate. For example, D_0 crystals would not be expected to grow at all for $\sigma_\infty < 10\%$ at -30°C based on these estimates, and D_1 crystals would grow only on the faces with dislocations. Note that this latter possibility could produce plates in the nominal "column" temperature range ($T < -22$°C), or columns in the "plate" range ($-22° < T < -10$°C), as is sometimes observed. Experimentally distinguishing between D_2, D_1, and D_0 crystals on the basis of shape should be much easier at low temperatures.

To compare our model predictions with observations of ice crystal stability limits, we have taken from *Kobayashi*'s [1965] diagram (see Figure 1) the line sep-

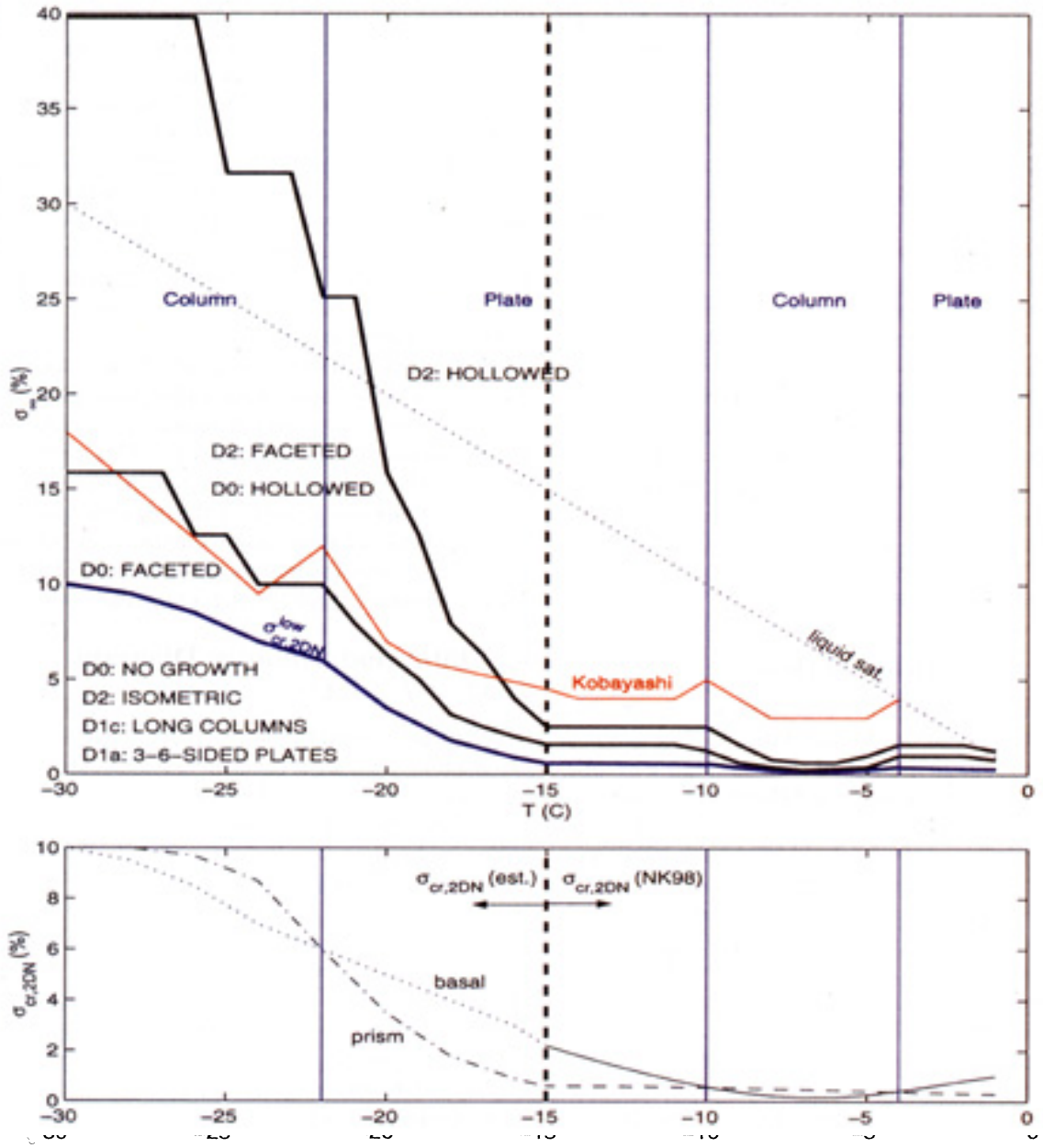

Plate 3. Conjectured habit diagram (top) for ice crystals as a function of temperature (T) and ambient supersaturation (σ_∞) predicted by our model using values of $\sigma^c_{cr,2D}$ and $\sigma^a_{cr,2D}$ (bottom) based on the [*Nelson and Knight*, 1998] (NK98) measurements for $T > -15°$C and our estimated extension of these values to lower temperatures based on field observations. In the top panel, the thick blue line indicates the lower of the $\sigma_{cr,2D}$ values at each temperature. The type of growth expected for each crystal type in the region $\sigma_\infty < \sigma^{low}_{cr,2D}$ is denoted. The thick solid black lines indicate our model-calculated stability limits for faceted growth of (lower) D_0 and (higher) D_2 crystals. For comparison, the red line indicates the observed stability limit suggested by the Kobayashi habit diagram (see Figure 1). The straight diagonal dotted line indicates the ice supersaturation in vapor saturated with respect to supercooled liquid water. The vertical blue lines mark the temperatures at which transitions between planar and columnar habits would be predicted to occur (when $\sigma_\infty > \sigma^{low}_{cr,2D}$).

arating the "solid" crystal regime from the hollow or "skeleton" regime, and replotted it in Plate 3. At temperatures above −15°C, Kobayashi's observed limit is closer to, but somewhat higher than, our predictions for D_2 crystals, and has a remarkably similar shape. Below −15°, Kobayashi's limit matches very closely our predicted stability limit for D_0 crystals. Although our model results can only be as accurate as the input values of $\sigma_{cr,2D}$, this comparison suggests that ice crystals may contain fewer dislocations at lower temperatures.

The fact that facets appear to be more stable than we have predicted at $T \geq -15$°C, where $\sigma_{cr,2D}$ has been measured, could be due either to the difficulties of detecting this limit observationally or to processes we have not included, or treated correctly, in our model. Perhaps the hollows are not noticeable until σ_∞ is significantly greater than σ_∞^{hol}, although this would bias the observations at all temperatures, not just above −15°C. Another experimental difficulty is measuring or maintaining the supersaturation accurately at values below liquid water saturation. This could be more of a problem at higher temperatures because the stability limits are lower, but one might expect values both greater than and less than the theoretical values in this case. In our model the only way to increase crystal stability would be to suppress 2-D nucleation at the corners. This could be an effect of impurities, which we have not included in our model. Alternatively, this could be an effect of steps generated by dislocations near the center of the face which move toward the corners and may disrupt subcritical 2-D nuclei, an effect not included in our simplified treatment of 2-D nucleation kinetics. If our supposition that ice crystals have fewer dislocations at lower temperatures is correct, then this effect would also decrease with temperature.

7. Cloud Model

Because of its speed, our single-crystal growth code can be inserted into dynamical models of ice clouds to calculate growth rates and shape evolution of the ice crystals. We have shown in previous sections that for a fixed set of environmental conditions, different assumptions about the surface kinetic mechanisms and parameters can lead to significantly different predictions for both growth rate and crystal shape. In clouds, conditions are constantly changing, and there can be strong feedbacks between condensation rates, the ambient supersaturation, and particle number densities (since nucleation rates are dependent on σ_∞). Therefore ice crystal microphysics could have important macroscopic effects on cloud evolution in addition to its control of the shape and consequent radiative properties of cloud ice. A full treatment of this problem is beyond the scope of this paper, but we can show some of the potential effects of including surface kinetics by using our growth code in a simple parcel cloud model. The calculations described in this section are not meant to realistically simulate cloud evolution, but serve only to illustrate the importance of these effects.

In our simplified cloud model, we prescribe an updraft velocity and ice crystal number density (we have considered only fully glaciated clouds) and calculate the evolution of temperature, supersaturation, and ice crystal size and shape as they grow and release latent heat. We have taken the number density of ice crystals to be 10^6 m^{-3}, which is toward the upper end of the range of observed number densities in real clouds (typically 10^3-10^7 m^{-3}) [*Pruppacher and Klett*, 1997; *Strom et al.*, 1997], in order to provide a noticeable sink for water vapor. We assume all of the crystals have identical size, shape, and surface characteristics, as they evolve with time. We have not included nucleation of new particles, so the number density of particles remains constant. We have also ignored radiative and ventilation effects on growth, but these are small for the small crystal sizes considered.

Our results for two cloud cases are discussed below. In each case we have calculated the evolution of the environmental conditions (T and σ_∞) and ice crystal characteristics ($\dot{a}, \dot{c}, a, c, \Gamma, m$) during the updraft using (1) our hexagonal crystal model assuming D_2, D_0, and D_1 crystals, and (2) the capacitance model. We assume the hexagonal crystals are initially isometric and determine the subsequent aspect ratio evolution self-consistently from the calculated values of $\dot{a}$ and $\dot{c}$. For the capacitance model we use a formula for the aspect ratio as a function of temperature taken from *Chen and Lamb* [1994], and we reduce the calculated mass growth rate by 18% to compensate for the larger radii (a and c) of an equivalent volume ellipsoid (see section 4.1).

7.1. Case 1: High Temperature

In Figure 11, we follow the evolution of a cloud of ice crystals in a 20 cm/s updraft starting at $T = -13$°C, as predicted by our model and by the capacitance model. We assume the temperature dependence of $\sigma_{cr,2D}$ given in Figure 7, and $\sigma_{SD} = \sigma_{cr,2D}$.

7.1.1. Supersaturation and crystal mass. The ambient supersaturation increases due to cooling until crystals become large enough to be an effective vapor sink, then decreases. The peak supersaturation value reached depends on the model, being highest for the model with the largest surface kinetic resistance (D_0) and smallest for the model with zero surface kinetic resistance (capacitance). The mass evolutions predicted by all of the models are very similar, so that in this case, an increase in surface kinetic resistance is compensated for by an increase in supersaturation. This supersaturation difference could have an indirect impact on mass evolution if it affected ice nucleation rates.

7.1.2. Crystal shape. The models predict very different crystal aspect ratio evolutions. The results seen here could have been anticipated based on our "steady state" habit calculations shown in Figure 10.

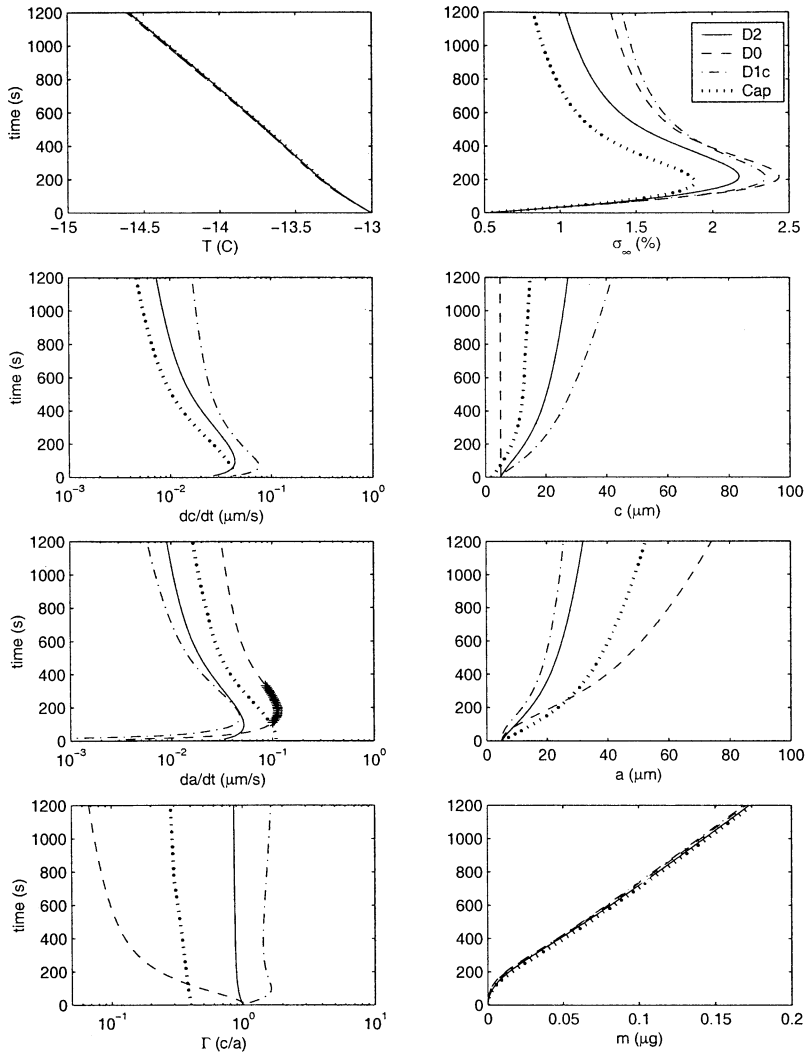

Figure 11. Evolution of ambient conditions and ice crystal characteristics for parcel model of a fully glaciated cloud (w = 20 cm/s, $N = 10^6$ m^{-3}, p = 500 mbar) comparing four ice crystal growth models: our hexagonal models for type D_2 (solid lines), D_0 (dashed lines), and D_{1c} (dash-dotted lines) crystals, and the capacitance model for ellipsoids with temperature-dependent aspect ratio (dotted lines). We have indicated conditions where our model predicts hollowing, and on which face, by cross-hatching the corresponding linear growth velocity lines.

The D_0 crystals become very platelike, with Γ becoming less than 0.1, because σ_∞ never exceeds $\sigma^c_{cr,2D}$, but the D_2 crystals remain isometric because the basal faces can grow by SDG. (Note also that our model predicts D_0 crystals would hollow on the prism faces during the brief period of time that $\sigma_\infty > \sigma^{hol}_\infty$.) Type D_{1c} crystals become moderately columnar with $1 < \Gamma < 2$. The aspect ratio expected at these temperatures based on *Chen and Lamb*'s [1994] $\Gamma(T)$ function is 0.3-0.4, but this represents an average of observed values which ranged from 0.15 to 0.85.

7.2. Case 2: Low Temperature

We have also run our parcel model for the case of an ice cloud at around -25°C with an updraft velocity of 35 cm/s. Unlike the last case which was initialized at equilibrium, here we assumed the initial vapor density was saturated with respect to liquid water, as it would be if the cloud had just glaciated. Application of our crystal growth model below -15°C is hampered by the lack of data regarding $\sigma_{cr,2D}$ at these temperatures. Therefore we have used the values inferred from observations, as discussed in section 5. We have also assumed $\sigma_{SD} = 2\%$ based on the results of *Sei and Gonda* [1989]. With these assumptions regarding the crystal surface properties, we have calculated the cloud evolution for D_2, D_1, and D_0 crystals, and the capacitance model, as shown in Figure 12. In this case the evolution of every one of our test parameters differs significantly from model to model, highlighting the importance of ice crystal surface characteristics in low-temperature clouds.

7.2.1. Supersaturation and crystal mass. Here the supersaturation decreases rapidly as crystals take up excess vapor, then reaches a nearly steady value af-

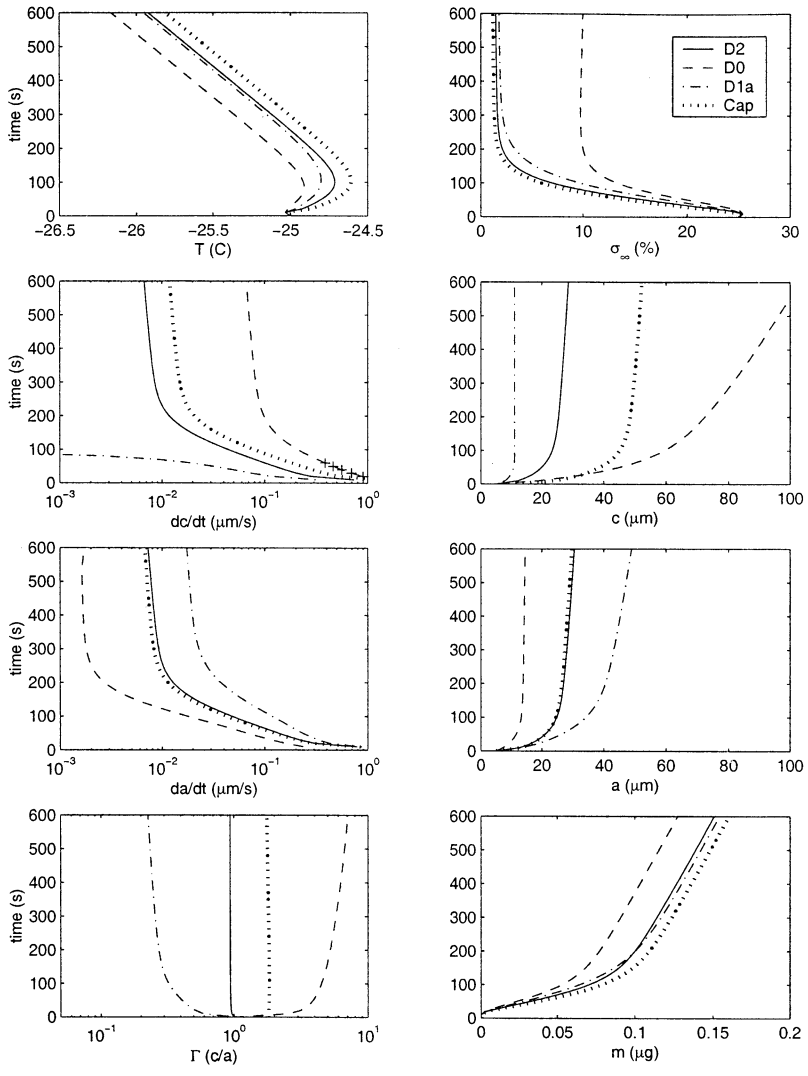

Figure 12. Same format as Figure 11 for cold ice cloud ($w = 35$ cm/s; $N_{ice} = 10^6\ m^{-3}$, $p = 330$ mbar), except we have used type D_{1a} crystals instead of type D_{1c}. The values used for the ice surface parameters were $\sigma^c_{cr,2D} = 8\%$, $\sigma^a_{cr,2D} = 9\%$ (see Figure 3), and $\sigma_{SD} = 2\%$.

ter a few minutes. This value is $\simeq 2\%$ for all cases except type D_0 crystals due to the high values assumed for $\sigma_{cr,2D}$ at this temperature. The mass evolution is also similar for each model except for the D_0 crystals which grew significantly slower. This is due to the fact that the prism faces were barely growing, so that the surface area of the growing basal faces remained constant; that is, the crystal was growing only in one dimension. This case shows that the supersaturation does not always compensate for surface kinetic effects on mass growth rates.

7.2.2. Crystal shape. As in the previous case, the predicted shape evolution is also dramatically different for each crystal type. Type D_{1a} crystals (which have dislocations on only the prism faces) attained an aspect ratio of almost 0.2 after 10 minutes, compared to 7 for D_0 crystals, and near 1 for D_2 crystals. The average observed value used for the capacitance model was about 2. These results demonstrate that both plates and columns can form at the same temperature, depending on the distribution of dislocations on the crystals.

8. Summary and Conclusions

This paper deals with two important, strongly coupled aspects of vapor growth of atmospheric ice crystals that have been largely neglected by previous models: shape and surface kinetics. We have developed one of the first models for three-dimensional faceted crystals to take both of these into account in a physical and self-consistent way. It is the first model capable of calculating the axial growth rates and the surface distributions of supersaturation and condensation coefficient on realistically shaped, three-dimensional, faceted ice crystals. The model is based on a novel, efficient nu-

merical method for solution of the exterior boundary value problem in three dimensions. We provide a first step in relating the observed macroscopic features of ice crystals to the surface processes by which they grow. Our major results are summarized below.

8.1. Growth Rates

8.1.1. Effect of shape. For hexagonal prism ice crystals with the same mass but different aspect ratio ($\Gamma = c/a$), the mass growth rate $\dot{m}$ is smallest for isometric crystals and increases for more columnar or planar shapes, such that $\dot{m}$ is $\approx 20\%$ higher for $\Gamma = 5$ and $\Gamma = 0.2$.

In cases where the surface kinetic resistance is low ($\sigma_\infty > \sigma_{cr,2D}$), the capacitance model predicts mass growth rates $10 - 20\%$ higher than our model predicts for hexagonal crystals of the same aspect ratio and mass. This difference is not strongly dependent on Γ, so reducing the ellipsoid capacitance model predictions in each case by 18% yields $\dot{m}$ values that are within 5% of our hexagonal crystal model.

The equivalent mass sphere model produces mass growth rates at least 10% higher than our model predictions for isometric hexagonal crystals.

8.1.2. Effect of surface kinetics. The mass growth rates of ice crystals can be significantly slowed due to surface kinetics (the processes by which adsorbed molecules become incorporated into the crystal lattice) if dislocations are absent and the ambient supersaturation is less than a few times the minimum critical supersaturation for 2-D nucleation, or even if dislocations are present and σ_∞ is also $\ll \sigma_{SD}$, the characteristic supersaturation for SDG.

8.2. Stability Limits for Faceted Growth

For crystals with no dislocations (type D_0) which grow only by 2-D nucleation, faceted growth becomes unstable when the ambient supersaturation reaches a value of 2-3 times $\sigma^{low}_{cr,2D}$, the lower of the critical supersaturations on the basal or prism faces. For crystals with dislocations on each face (type D_2), faceted growth remains stable at larger supersaturations, with hollowing beginning at 4 to 5 times $\sigma^{low}_{cr,2D}$. The stability limit for type D_1 crystals depends on whether the dislocations are on the face with the lower or higher value of $\sigma_{cr,2D}$, making the D_1 crystals the same as D_0 or D_2 crystals, respectively. As the value of $\sigma_{cr,2D}$ for each face varies with temperature, so will the absolute value of σ^{hol}_∞. For $T \geq -15°C$, *Nelson and Knight*'s [1998] measurements of $\sigma_{cr,2D}$ predict σ^{hol}_∞ varies from 0.6 to 2.7%. Therefore under conditions of water saturation in mixed phase clouds, nonfaceted growth is predicted by our model, as observed. The frequent occurrence of unhollowed crystals at the low temperatures and relatively high supersaturations of the Arctic and Antarctic suggests that critical supersaturations are of the order of 10% at temperatures below about $-20°C$. Therefore σ^{hol}_∞ could range from 20% to 50%.

8.3. Interpretation of Particle Shapes

Based on the results of our model, it is possible to use observed shapes of ice crystal crystals in the atmosphere, particularly if the growth conditions (T, σ_∞) are also measured, to derive information regarding the nature of the ice crystal surface, including the critical supersaturations for 2-D nucleation, the abundance and distribution of dislocations, and related to these, the crystal growth mechanism(s). Ideally, of course, we would like to do this in reverse, and use our model to predict the shapes and sizes of atmospheric ice crystals for given environmental conditions. However, this is not yet possible due, in large part, to our lack of knowledge regarding the physical nature of the ice crystal surface. Therefore this "postdiction" of crystal characteristics

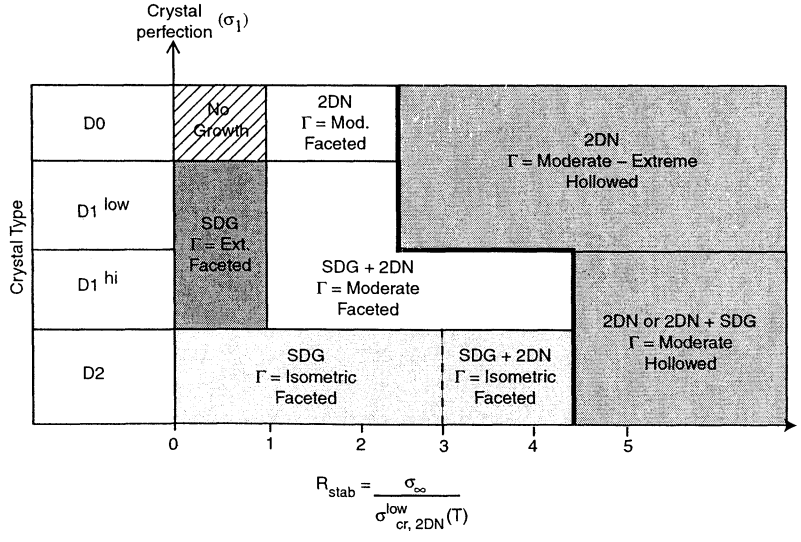

Figure 13. Diagram summarizing our results for the expected shape stability, aspect ratio, and growth mechanisms for ice crystals of each type (D_2, D_1, and D_0) as a function of $R_{stab} = \sigma_\infty / \sigma^{low}_{cr,2D}$.

from shape is an important exercise, as is the collection of more in situ and laboratory data.

Figure 13 summarizes our results for the expected shape stability, aspect ratio, and growth mechanisms for ice crystals of each type (D_2, D_1, and D_0) as a function of $R_{stab} = \sigma_\infty / \sigma_{cr,2D}^{low}$. This diagram shows the stability limit separating faceted and hollowed crystals for each crystal type as described above. We have characterized the aspect ratio of faceted crystals as isometric, moderate, or extreme ($\Gamma > 10$). Isometric crystals are most likely to be type D_2, with dislocations on each face. Crystals with extreme aspect ratios ($\Gamma \geq 10$), such as the long "whiskers" observed in the Antarctic, are probably type D_{1c}, with dislocations completely absent on prism faces. The occurrence of these crystals implies that the supersaturation must be less than $\sigma_{cr,2D}$ on the nongrowing face, so that lower limits for $\sigma_{cr,2D}$ at these temperatures can be determined if σ_∞ is known. As can be seen in this diagram, the regime most sensitive to the presence and distribution of dislocations is $0 < \sigma_\infty < \sigma_{cr,2D}^{low}$; no growth implies D_0, growth to extreme Γ implies D_1, and more isometric growth implies D_2 type crystals. This regime may be much more accessible experimentally at very low temperatures.

8.4. Effects of Surface Kinetics on Cloud Evolution

Different assumptions regarding the characteristics of the ice crystal surface, such as the distribution of dislocations, can lead to very different predictions for particle shapes in clouds, and hence, possibly inaccurate predictions of radiative effects and precipitation formation. At low temperatures the effect of surface impedance on crystal growth may be enough to substantially increase supersaturations in fully glaciated clouds, which may have important effects on new particle nucleation rates, and can also decrease the mass growth rate. The capacitance model, which does not include surface kinetic effects, will generally underestimate the supersaturation in condensing ice clouds.

Acknowledgments. This research was supported by NSF grant ATM-97-04156. We are grateful to A. Korolev and A. Heymsfield for providing us with data from their field studies, to Brian Swanson and Neil Bacon for insightful comments, and to Jon Nelson for very helpful discussions and ideas. For permission to reproduce the Kobayashi diagram (Figure 1), we thank Taylor & Francis Ltd., PO Box 25, Abingdon, Oxfordshire, OX14 3UE, UK.

References

Atkinson K., Two-grid iteration methods for linear integral equations of the second kind on piecewise smooth surfaces in $\mathbf{R}^3$, *SIAM J. Sci. Stat. Comput., 15*, 1083-1104, 1994.

Atkinson K., User's Guide to a Boundary Element Package for Solving Integral Equations on Piecewise Smooth Surfaces, *Rep. Comput. Math. 103*, Dep. of Math., Univ. of Iowa, Iowa City, 1999.

Auer, A. H., and D. L. Veal, The dimensions of ice crystals in natural clouds, *J. Atmos. Sci., 27*, 919-926, 1970.

Bacon, N. J., B. D. Swanson, M. B. Baker, and E. J. Davis, Low-temperature electrodynamic balance study of the evolution and growth rates of supercooled water droplets and ice particles, *Proc. Int. Conf. Clouds Precip., 13th*, 673-676, 2000.

Baker, M. B., Cloud microphysics and climate, *Science, 276*, 1072-1078, 1987.

Burton, W., N. Cabrera and F. Frank, The growth of crystals and the equilibrium structure of their surfaces, *Proc. R. Soc. London, ser. A 243*, 299-358, 1951.

Chen, J., and D. Lamb, The theoretical basis for the parameterization of ice crystal habits: Growth by vapor deposition, *J. Atmos. Sci. 51*, 1206-1221, 1994.

Curry, J. A., F. G. Meyer, L. F. Radke, C. A. Brock, and E. E. Ebert, Occurrence and characteristics of lower tropospheric ice crystals in the Arctic, *Int. J. Climatol., 10*, 749-764, 1990.

Frank, F. C., Snow crystals, *Contemp. Phys. 23*, 3-22, 1982.

Fukuta, N., and Q. J. Lu, Surface microphysical mechanism for ice crystal growth habit development, *Atmos. Res. 32*, 31-43, 1994.

Greengard, L., and V. Rohklin, A new version of the fast multipole method for the Laplace equation in three dimensions, *Acta Numer., 6*, 229, 1997.

Heymsfield, A. J., K. M. Miller, and J. D. Spinhirne, The 27-28 October 1986 FIRE IFO cirrus case study: Cloud microstructure, *Mon. Weather Rev., 118*, 2313-2328, 1990.

Jensen, E. J., O. B. Toon, D. L. Westphal, S. Kinne, and A. J. Heymsfield, Microphysical modeling of cirrus, 1, Comparison with 1986 FIRE IFO measurements, *J. Geophys. Res., 99*, 10,421-10,442, 1994a.

Jensen, E. J., O. B. Toon, D. L. Westphal, S. Kinne, and A. J. Heymsfield, Microphysical modeling of cirrus, 2, Sensitivity studies, *J. Geophys. Res., 99*, 10,443-10,454, 1994b.

Kaldis, E., Principles of the vapour growth of single crystals, in *Crystal Growth: Theory and Techniques*, edited by C. H. L. Goodman, vol. 1, chap. 2, Plenum, New York, 1974.

Kikuchi, K., and A. W. Hogan, Properties of diamond dust type crystals observed in summer season at Amundsen-Scott South Pole Station, Antarctica, *J. Meteorol. Soc. Jpn., 57*, 180-189, 1979.

Kobayashi, T., On the variation of ice crystal habit with temperature, *Physics of Snow and Ice*, Part I, edited by H. Oura, pp. 95-104, Hokkaido Univ., Sapporo, Japan, 1965.

Korolev, A., G. Isaac, and J. Hallett, Ice particle habits in Arctic clouds, *Geophys. Res. Lett. 26*, 1299-1302, 1999.

Kuroda, T., Rate determining processes of growth of ice crystals from the vapour phase, I, Theoretical consideration, *J. Meteorol. Soc. Jpn., 62*, 552-561, 1984.

Kuroda, T., and R. Lacmann, Growth kinetics of ice from the vapour phase and its growth forms, *J. Cryst. Growth, 56*, 189-205, 1982.

Libbrecht, K. G., Cylindrically symmetric Green's function approach for modeling the crystal growth morphology of ice, *Phys. Rev. E. 60*, 1967-1974, 1999.

Magono, C., and C. W. Lee, Meteorological classification of natural snow crystals, *J. Fac. Sci. Hokkaido Univ., Ser. 7(2)*, 321, 1966.

Mason, B. J., *The Physics of Clouds*, Clarendon, Oxford, England, 1971.

McKnight, C. V., and J. Hallett, X-ray topographic studies of dislocations in vapor-grown ice crystals, *J. Glaciol., 21*, 397-407, 1978.

Nakaya, U., M. Hanajima and J. Mugurama, Physical investigations of the growth of snow crystals, *J. Fac. Sci. Hokkaido Univ., Ser. 2, 5(3)*, 88, 1958.

Nelson, J., A theoretical study of ice crystal growth in the atmosphere, Ph.D. dissertation, Univ. of Wash., Seattle, 1994.

Nelson, J., and M. Baker, A new theoretical framework for studies of vapor growth and sublimation of small ice crystals in the atmosphere, *J. Geophys. Res., 101*, 7033-7047, 1996.

Nelson, J., and C. A. Knight, Snow crystal habit changes explained by layer nucleation, *J. Atmos. Sci., 55*, 1452-1465, 1998.

Pruppacher, H., and J. D. Klett, *Microphysics of Clouds and Precipitation*, Kluwer Acad., Norwell, Mass., 1997.

Sei, T., and T. Gonda, The growth mechanism and the habit change of ice crystals growing from the vapor phase, *J. Cryst. Growth, 94*, 697-707, 1989.

Strom, J., B. Strauss, T. Anderson, F. Schroder, J. Heintzenberg, and P. Wendling, In situ observations of the microphysical properties of young cirrus clouds, *J. Atmos. Sci., 54*, 2542-2553, 1997.

Vogelmann, A. M., and T. P. Ackerman, Relating cirrus cloud properties to observed fluxes: A critical assessment, *J. Atmos. Sci., 52*, 4285-4301, 1995.

Wood, S. E., Nucleation and growth of CO_2 ice crystals in the Martian atmosphere, Ph.D. dissertation, Univ. of Calif., Los Angeles, 1999.

Yamashita, A., On the trigonal growth of ice crystals, *J. Meteor. Soc. Jpn., 51*, 307-317, 1973.

Yokoyama, E., and T. Kuroda, Pattern formation in growth of snow crystals occurring in the surface kinetic process and the diffusion process, *Phys. Rev. A, 41*, 2038-2049, 1989.

M. B. Baker and S. E. Wood, Geophysics Program, University of Washington, Box 351650, Seattle, WA 98195-1650. (sewood@atmos.washington.edu)

D. Calhoun, Department of Computer Science, Courant Institute of Mathematical Sciences, New York University, 251 Mercer Street, New York, NY 10012-1185.

(Received February 9, 2000; revised May 18, 2000; accepted May 24, 2000.)